NAVAL POSTGRADUATE SCHOOL
Monterey , California

UNITED STATES NAVY · NAVAL POSTGRADUATE SCHOOL ·

THESIS

MATCHED FIELD PROCESSING IN SHALLOW WATER USING A SMALL APERTURE HORIZONTAL LINE ARRAY

by

Robert S. Veenhuis

December 1994

Thesis Advisor: James H. Wilson

Approved for public release; distribution is unlimited

REPORT DOCUMENTATION PAGE

Form Approved
OMB No. 0704-0188

1. AGENCY USE ONLY (LEAVE blank)	2. REPORT DATE DEC 1994	3. REPORT TYPE AND DATES COVERED Master's Thesis

4. TITLE AND SUBTITLE	5. FUNDING NUMBERS
Matched Field Processing in Shallow Water Using a Small Aperture Horizontal Line Array	

6. AUTHOR(S)

Robert S. Veenhuis

7. PERFORMING ORGANIZATION NAME(S) AND ADDRESS(ES)	8. PERFORMING ORGANIZATION REPORT NUMBER
Naval Postgraduate School Monterey, CA 93943-5000	

9. SPONSORING / MONITORING AGENCY NAME(S) AND ADDRESSES	10. SPONSORING/ MONITORING AGENCY REPORT NUMBER

11. SUPPLEMENTARY NOTES

The views expressed in this thesis are those of the author and do not reflect the official policy or position of the Department of Defense or the U.S. Government.

12a. DISTRIBUTION / AVAILABILITY STATEMENT	12b. DISTRIBUTION CODE
Approved for public release; distribution is unlimited	

13. ABSTRACT (Maximum 200 words)

Matched field processing (MFP) is a beamforming technique which allows for the detection and localization of an acoustic source in range and depth using passive sonar. The performance of MFP in shallow water environments using a short aperture horizontal line array is investigated. Shallow water test cases are utilized to evaluate the effects of frequency, bottom type, relative target bearing, and sound speed profile on MFP performance. Data from RANGEX 1-92 is also utilized to test the performance of the eight nearest neighbor peak picker (ENNPP) and M of N tracker for a horizontal line array in a real ocean environment.

It is shown that MFP performance is significantly better for higher frequencies, for more reflective bottom types, and for relative target bearings away from the broadside beams. It is also shown that the performance of plane wave beamformers is severely degraded in shallow water for relative bearings away from the broadside beams, particularly at higher frequencies. Finally, the MFP algorithm in conjunction with the ENNPP and M of N tracker are shown to perform well in the real ocean environment.

14. SUBJECT TERMS		15. NUMBER OF PAGES 94
Matched Field Processing, Plane Wave Beamforming, M of N Tracker		16. PRICE CODE

17. SECURITY CLASSIFICATION OF REPORT Unclassified	18. SECURITY CLASSIFICATION OF THIS PAGE Unclassified	19. SECURITY CLASSIFICATION OF ABSTRACT Unclassified	20. LIMITATION OF ABSTRACT UL

ii

Approved for public release; distribution is unlimited

MATCHED FIELD PROCESSING IN SHALLOW WATER USING A SMALL APERTURE HORIZONTAL LINE ARRAY

Robert S. Veenhuis
Lieutenant Commander, United States Navy
B.A., Hamline University, 1982

Submitted in partial fulfillment of the
requirements for the degree of

MASTER OF SCIENCE IN METEOROLOGY AND PHYSICAL OCEANOGRAPHY

from the

NAVAL POSTGRADUATE SCHOOL
DECEMBER 1994

Author: _____
Robert S. Veenhuis

Approved by: _____
James H. Wilson, Thesis Advisor

_____
Ching-Sang Chiu, Second Reader

_____
Robert H. Bourke, Chairman,
Department of Oceanography

iii

ABSTRACT

Matched field processing (MFP) is a beamforming technique which allows for the detection and localization of an acoustic source in range and depth using passive sonar. The performance of MFP in shallow water environments using a short aperture horizontal line array is investigated. Shallow water test cases are utilized to evaluate the effects of frequency, bottom type, relative target bearing, and sound speed profile on MFP performance. Data from RANGEX 1-92 is also utilized to test the performance of the eight nearest neighbor peak picker (ENNPP) and M of N tracker for a horizontal line array in a real ocean environment.

It is shown that MFP performance is significantly better for higher frequencies, for more reflective bottom types, and for relative target bearings away from the broadside beams. It is also shown that the performance of plane wave beamformers is severely degraded in shallow water for relative bearings away from the broadside beams, particularly at higher frequencies. Finally, the MFP algorithm in conjunction with the ENNPP and M of N tracker are shown to perform well in the real ocean environment.

TABLE OF CONTENTS

ACKNOWLEDGEMENTS

The author would like to thank Professor James H. Wilson for his tireless support and assistance in researching and preparing this thesis.

I. INTRODUCTION

A. BACKGROUND

The original intent of this thesis was to investigate the feasibility of utilizing matched field processing (MFP) [Ref. 1-15] as a ranging technique for submarines operating in shallow water. MFP is an alternative beamforming method to plane wave beamforming which would allow submarines to conduct "single leg" target motion analysis using a short aperture horizontal line array. However, during the conduct of the analyses for this thesis, it was discovered that in shallow water environments, plane wave beamformers for horizontal line arrays suffer a significant fundamental signal coherence degradation. Since all of the Navy's operational sonars for horizontal line arrays use plane wave beamforming, this is considered a significant problem for anticipated shallow water operations. MFP should therefore be regarded not only as a supplement to plane wave beamforming, but also as a necessary compliment to conventional plane wave beamformers with horizontal line arrays in shallow water.

The problem of signal coherence degradation is the result of normal mode propagation in shallow water environments, which causes reduced signal coherence in those beams where the signal is not estimated well by a single plane wave. The problem is illustrated in Fig. 1.1 for a 48 element, equally spaced horizontal line array, where beamformer output is plotted as a function of range for a range independent, isospeed medium with a hard, reflective bottom and a water depth of 100 m. The magnitude of the beamformer output for this plot is directly proportional to the plane wave signal coherence. Figure 1.1(a) shows that for a relative target bearing of 90^0 (i.e., broadside),

1

o 138 Hz   * 662 Hz

(a) Relative bearing = 90⁰ 　　　　　　 (b) Relative bearing = 60⁰

(c) Relative bearing = 30⁰ 　　　　　　 (d) Relative bearing = 0⁰
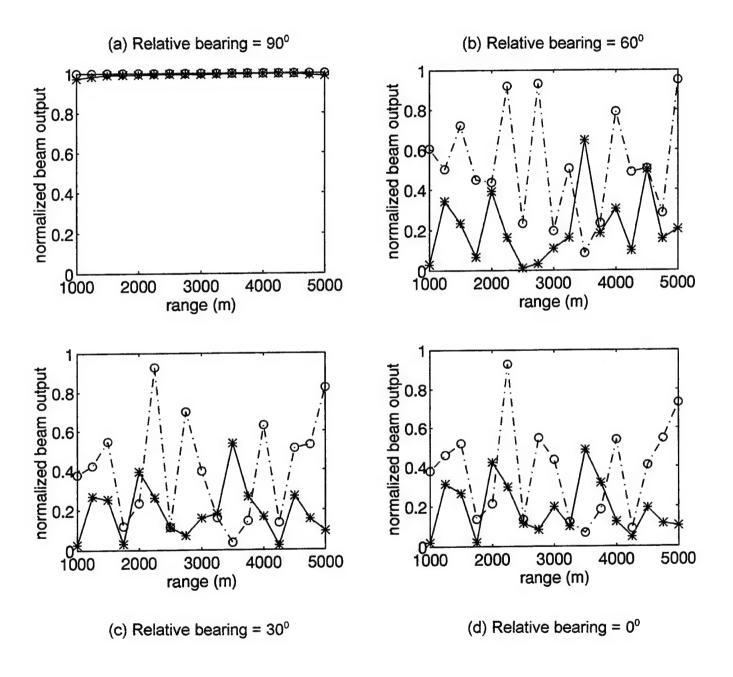
Figure 1.1 Normalized beam outputs vs. range for various relative bearings.

the plane wave signal coherence is very good. This is because the distance from the source to each hydrophone is very nearly the same for all of the array hydrophones when the array is broadside to the source, thus causing the acoustic signal to be in phase over the entire array aperture. However, as the target relative bearings get closer to 0^0 (i.e., end-fire) as shown in plots (b-d), the plane wave signal coherence decreases significantly, especially at 662 Hz. This indicates that the normal mode solution to the wave equation is significantly different from a plane wave when the range from each hydrophone to the source varies across the array. Based on this result, the performance of plane wave beamformers in shallow water is considered questionable, thereby prompting research into alternative beamforming methods for shallow water operations.

B. REVIEW OF CONVENTIONAL SUBMARINE TMA

Submarine target motion analysis (TMA) with passive sonar has traditionally been accomplished by conducting a series of maneuvers while measuring the target's bearings and bearing rates, and then estimating the target's course, speed and range by utilizing various plots and equations. This method has been highly successful against nuclear submarines and surface warships operating in the open ocean where the ray mode assumption is valid, thereby facilitating the use of conventional plane wave beamformers. However, the end of the cold war and the increased threat of diesel submarines from third world countries has stimulated interest in passive ranging methods which are reliable against submerged diesel submarines in shallow water. As was previously discussed, this is a complex acoustic problem due to the normal mode characteristics of shallow water

3

environments, which severely degrade the performance of conventional plane wave beamformers. Also, the restricted maneuverability in shallow water makes multiple leg TMA extremely difficult, particularly when a towed array is utilized.

Matched field processing (MFP) is a promising solution to this problem because the MFP algorithm requires no course changes and it utilizes the multiple acoustic arrival paths of shallow water environments to estimate target bearing, range and depth. Although the excessive computer processing requirements made this method impractical when it was first developed, recent improvements in computer hardware and software technology have made MFP both possible and relatively easy to perform in real time. The Navy's approved high speed shipboard computer, the DTIC 4, is a VME bus processor which is fast enough to perform the MFP calculations in real time, and is also compact enough to fit easily into the Sonar Equipment Space or any other suitable area on board ship. These advancements in technology have made MFP a viable beamforming method for shallow water operations.

C. OBJECTIVE

The objective of this thesis is to assess the performance of MFP with a short aperture horizontal line array in shallow water. The MFP algorithm will be tested in a variety of shallow water environments (100 m water depth) by mathematically constructing a series of simulated targets and then attempting to track these targets using MFP. These shallow water test cases allow for an evaluation of MFP performance in shallow water in the absence of real data.

4

In addition to the shallow water test cases, data from a deep water test site will be used to evaluate the specific MFP algorithm described later in this thesis. The data set is from RANGEX 1-92, conducted on an instrumented range in December 1991 near Kauai, Hawaii, in 2500 to 3000 m of water. During this exercise acoustic measurements were obtained by a submerged submarine using towed array against another submerged submarine. The ground truth values of target bearing, range, depth, course and speed were well documented and will be compared to the calculated MFP values.

II. ACOUSTIC PROPAGATION CHARACTERISTICS

A. REVIEW OF DEEP WATER ACOUSTIC PROPAGATION

In deep water environments signal transmission loss (TL) and horizontal signal coherence are measured, analyzed, and modeled as separate acoustic parameters. In the 1970's and 1980's, horizontal signal coherence proved to be sufficient to support the use of very long arrays, as evidenced by a successful experiment with a towed array three times the length of a SURTASS array (also referred to as the 3X array). The results of this experiment [Ref. 16] showed that high signal coherence allowed beamforming over the entire 3X array aperture. Array signal gain (ASG) is usually assumed to be ideal (20 log M), where "M" is the number of elements in an equally space line array.

TL modeling has received a great deal of attention in deep water, with the development of very sophisticated and successful TL models such as the Parabolic Equation (PE), ASTRAL, and the Finite Element Parabolic Equation (FEPE). The bottom interacting energy is of relatively minor importance in deep water because this energy is dominant at ranges between the direct path and first convergence zone (CZ) and also between successive CZ's. The TL levels from bottom interacting paths are very high and most often significantly greater than figure of merits (FOM) for typical threats of interest. Therefore, the bottom interacting paths do not generally impact sonar performance in deep water.

B. SHALLOW WATER ACOUSTIC PROPAGATION

In shallow water the previous discussion does not apply. Bottom interacting energy dominates signal propagation below 5 kHz in most shallow water areas, and may impact propagation well above 5 kHz. Both TL and horizontal signal coherence show high spatial variability and are impacted greatly by the geoacoustic properties of the bottom and sub-bottom in shallow water [Ref. 17-19]. Recent shallow water analyses [Ref. 20] have shown that TL amplitude fluctuations and signal coherence phase fluctuations are highly correlated as a function of range, and closely related to the bottom and sub-bottom geoacoustic properties. Furthermore, for ranges up to 15 km, TL amplitude fluctuations occur in the interval of current FOM's for shallow water diesel threats. The test cases in this thesis will also show that signal coherence phase fluctuations significantly impact ASG for plane wave beamformers, thus degrading the performance of plane wave beamformers in shallow water. As a result, signal coherence and TL must be evaluated jointly in diverse shallow water environments. Although MFP does not provide the solution in all circumstances, this thesis will show that it is a promising method of shallow water beamforming in many specific cases.

III. REVIEW OF BEAMFORMING

A. CONVENTIONAL TIME DOMAIN PLANE WAVE BEAMFORMING

Figure 2.1 shows a plane wave arriving at a line array with 'M', equally-spaced elements. If no time delays were applied, the signal would arrive sequentially at each hydrophone, thus producing output wave forms which would add incoherently due to
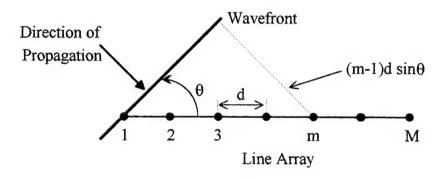
Figure 2.1 Geometry for signal field arriving at a line array.

their temporal offsets. However, if the hydrophones were "aligned" with fixed time delays and then summed (see Fig. 2.2 below), the signals would add coherently while the background noise would add incoherently, thus improving the SNR significantly. This process of time alignment, followed by summation, is called *time domain beamforming*
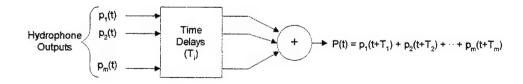
Figure 2.2 Conventional time domain beamformer block diagram.

9

[Ref. 21] and has been used in sonar systems developed since the 1960's, including the AN/BQQ-5 series. These systems simultaneously form beams in several directions by providing each hydrophone channel with a set of tapped delay elements. Time domain beamforming was the method of choice in the early digital sonar systems because the computer technology of the time was inadequate for performing the fast Fourier transforms required by frequency domain beamformers.

The major disadvantage of time domain beamformers is that additional hardware is required to increase the number of beams in the array, making the modification costly and labor intensive. With a frequency domain beamformer, the beam pattern can be modified relatively easily with a software change. This is important since it has been shown that array performance is significantly improved when the number of beams is increased well beyond the number provided by the AN/BQQ-5 series time domain beamformers.

B. FREQUENCY DOMAIN BEAMFORMING

1. Fourier Transforms

The purpose of Fourier analysis is to express a signal as a sum of sinusoidal functions. When the transformation is applied to a time dependent function, the result is a frequency domain representation of the signal. Conversely, application of the inverse transformation to the frequency domain signal reproduces the original time domain function. Many digital processing procedures are performed in the frequency domain because it is generally easier to express the signal, noise and system response in the

10

frequency domain. Also, digital methods for approximating Fourier transforms, known as fast Fourier transforms (FFT's), are available as a standard subroutine for computers.

a. Fourier Integral Transforms

For a time domain function, g(t), the Fourier integral is expressed as

$$G(f) = \int_{-\infty}^{\infty} g(t) \exp(-i2\pi ft)\, dt \qquad (2.1)$$

where G(f) is the frequency domain equivalent of g(t). Similarly, G(f) can be restored to the time domain with the inverse transform operation

$$g(t) = \int_{-\infty}^{\infty} G(f) \exp(i2\pi ft)\, df. \qquad (2.2)$$

The functions g(t) and G(f) are normally referred to as Fourier transform pairs. [Ref. 22, pp. 156-159]

b. Discrete Fourier Transforms

The Fourier integral expressions assume that the functions are continuous over the entire range from positive infinity to negative infinity. However, in the real world, only finite length records exist. Also, digital processing systems can analyze only those signals which have been converted to a discrete set of numbers. These constraints have led to the development of digital approximations to Fourier integral transforms known as discrete Fourier transforms (DFT's) [Ref 22, pp. 195-199].

The DFT can be performed on a function only if it has been digitized, as shown in Fig. 2.3. Let g(n) be the value associated with sample "n", and let G(k) be the

11
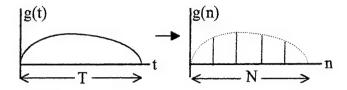
Figure 2.3 Analog to digital conversion.

corresponding frequency domain sample. Then the DFT pair is

$$G(k) = \sum_{n=0}^{N-1} g(n) W^{kn} \qquad (2.3)$$

$$g(n) = \frac{1}{N} \sum_{n=0}^{N-1} G(k) W^{-kn} \qquad (2.4)$$

where $W^{kn} = \exp\left(\frac{-i2\pi kn}{N+1}\right)$, N is the number of samples, and k is the frequency index.

Unfortunately, the DFT calculations can be computer intensive if N is large. For example, if N = 1000, the computation of G(k) for each discrete frequency, k, would require 1000 complex multiplications and 1000 complex additions, for a total of 1 million complex operations. The fast Fourier transform (FFT) algorithm was developed to provide a more efficient method for computing DFT's.

c. *Fast Fourier Transforms*

The FFT algorithm divides the summation for G(K) into two parts: one for the odd terms in 'n' and one for the even terms [Ref. 22, pp. 199-203]. If N is a power

12

of two, the expression for G(k) can then be rewritten as   .

$$G(k) = \sum_{n=0}^{\frac{N}{2}-1} g(2n)\, W^{2kn} + \sum_{n=0}^{\frac{N}{2}+1} g(2n+1)\, W^{k(2n+1)} \qquad (2.5)$$

Since each summation now generates only N/2 distinct values of G(k) rather than N values, the number of multiplications for each value of k is N/2 + N/2 + 1 = N + 1, and the total number of complex multiplications is N/2(N + 1) = N²/2 + N/2. This is a reduction in computations by nearly a factor of 2 compared to the direct DFT calculation. As long as N is a power of 2, each of the summations may be further subdivided into groups with N/4 points each, representing an additional reduction of approximately 2. This process may be repeated until only 2 terms are leftover in each summation. The total number of computations then becomes N/2 $\log_2$ N, which is a dramatic reduction in the number of computations. For example, if N = 1000, the FFT requires 4983 computations, far fewer than the 1 million computations for a DFT.

2. Phase Delay Frequency Domain Beamforming

Phase delay beamformers apply FFT's to the hydrophone time series and then introduce phase delays in the frequency domain which are mathematically equivalent to time delays in the time domain [Ref. 22, pp. 303-320; Ref. 23]. Referring again to Fig. 2.1, the phase of the mth element will be delayed relative to the phase of the first element by the time necessary for sound to travel the distance "(m-1)d sin θ"; thus, the phase delay (u_m) at the mth hydrophone for acoustic wavelength λ will be

$$u_m = \frac{2\pi m d}{\lambda} \sin \theta \; radians. \qquad (2.6)$$

When the phase delayed voltages for all elements are summed, as shown in Fig. 2.4, the resultant output voltage becomes

$$P(f) = p_1(f) + p_2(f)e^{iu_m} + p_3(f)e^{i2u_m} + \cdots + p_M(f)e^{i(M-1)u_m}. \qquad (2.7)$$
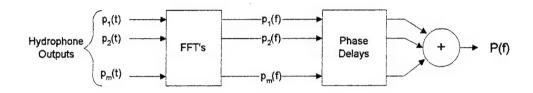
Figure 2.4 Conventional phase delay beamformer block diagram.

As stated previously, the principle advantage of this method is that the phase delays can be accomplished by software instead of hardware. This allows for simplified hardware design and greater flexibility in beamforming, since any number of beams can be formed in almost any direction with the appropriate software. This is advantageous because performance is improved by increasing the number of beams.

3. Covariance Matrix Frequency Domain Beamformer

This method utilizes the spatial coherence of the signal plus noise field by cross multiplying the FFT's of all sensor pairs [Ref. 22, pp. 406-413]. The collection of all such cross sensor FFT products in any frequency bin is called the *covariance matrix*. The advantage of this method is that it allows the application of various weighting factors to the matrix elements to enhance array gain. This covariance matrix is correlated with steering vectors to estimate the acoustic field directionality for each frequency bin. The

diagram for forming the covariance matrix is shown in Fig. 2.5, where f_i represents the ith frequency frequency bin, and $p_i^*(f_i)$ is the complex conjugate of $p_i(f_i)$. The covariance matrix is formed from the cross-products of the phase-delayed hydrophone FFT's and their complex conjugates. This FFT product for a given frequency bin will be shown as $v_j v_k^*$ in all further sections, and the covariance matrix operation will be represented as COV(f).

	Column 1	Column 2	$\cdot$ $\cdot$ $\cdot$	Column M
Row 1	$p_1(f_i)p_1^*(f_i)$	$p_1(f_i)p_2^*(f_i)$	$\cdot$ $\cdot$ $\cdot$	$p_1(f_i)p_m^*(f_i)$
Row 2	$p_2(f_i)p_1^*(f_i)$	$p_2(f_i)p_2^*(f_i)$	$\cdot$ $\cdot$ $\cdot$	$p_2(f_i)p_m^*(f_i)$
$\vdots$	$\vdots$	$\vdots$		$\vdots$
Row M	$p_m(f_i)p_1^*(f_i)$	$p_m(f_i)p_2^*(f_i)$	$\cdot$ $\cdot$ $\cdot$	$p_m(f_i)p_m^*(f_i)$
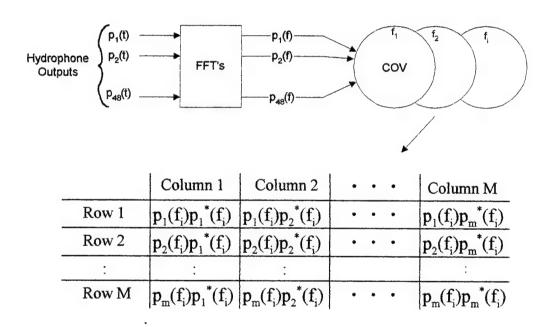
Figure 2.5 Covariance matrix for a single frequency bin.

Covariance matrix beamforming is accomplished by correlating the covariance matrix with complex plane wave steering vectors SV) and their transposes (SV^t), yielding a conventional beamforming output (B) which varies as a function of azimuth angle (θ) and frequency (f):

$$B(\theta,f) = [SV^t] \cdot [COV(f)] \cdot [SV] / M^2 \qquad (2.8)$$

15

where $\qquad SV = \begin{bmatrix} e^{iu} \\ e^{i2u} \\ . \\ e^{imu} \end{bmatrix}$ $\qquad$ and $\qquad SV^t = [e^{iu}\ e^{i2u} \cdots e^{imu}].$ $\qquad$ (2.9)

The value of B varies between 0 and 1, depending on how well the covariance matrix and the steering vector are correlated. To determine the arrival path for the incoming signal, the steering vector is slowly rotated in increments of θ , and new values of B are calculated for each θ and graphed, as shown in Fig. 2.6. The spike in the correlation curve indicates the arrival direction for the incoming plane wave signal.
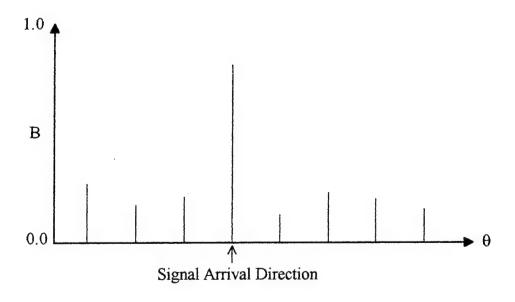
Figure 2.6 Covariance matrix correlation curve.

C. INVERSE BEAMFORMING (IBF)

IBF [Ref. 24-29] is a processing method which consists of three separate algorithms: a beamforming algorithm known as the *Fourier Integral Method*, a data thresholding algorithm called the *Eight Nearest Neighbor Peak Picker* (ENNPP), and a post processing algorithm called the *M of N Tracker*. The Fourier Integral Method (FIM) is a beamforming method designed to improve the array gain for a line array by applying various weighting factors to the covariance matrix elements. The method is described in Appendix A. The ENNPP and M of N tracker are described in the next chapter.

D. PROBLEMS WITH PLANE WAVE BEAMFORMING

The conventional beamforming methods previously discussed were developed for acoustic fields consisting of perfectly coherent plane wave signals in totally incoherent noise. These plane wave beamformers are the ideal choice for this simplistic acoustic environment, and in general, they perform well in conditions where the plane wave approximation is valid.

However, in most shallow water environments, the plane wave approximation is poor, since correlated multiple signals (multipaths) arrive from different elevation angles, and the ambient noise field is far from being spatially incoherent. Other plane wave beamforming algorithms, including FIM, Multiple Signal Classification (MUSIC) [Ref. 30], and the Minimum Variance Method [Ref. 31] have shown improved performance over conventional time delay and phase delay beamformers. But for submarines conducting TMA in shallow water, the preferred method is one which takes advantage of

17

these multiple arrival paths and also eliminates the need for course changes. A method

with high potential , MFP, will be discussed in the next chapter.

IV. MATCHED FIELD PROCESSING

A. INTRODUCTION

MFP determines target location by "matching" the measured acoustic pressure field at the hydrophone outputs to a predicted pressure field based on an assumed source location [Ref. 1-15]. The predicted acoustic field at the hydrophones is determined by using a suitable acoustic propagation model, such as the Generic Sonar Model (GSM) or CASS for deep water, or a fully-coupled, normal mode model for shallow water. These predictions, which vary with source location, are compared to the measured signal and noise coherence values to find the highest correlation. The basic block diagram for MFP is shown in Fig. 3.1. For optimum performance over the entire frequency range, plane
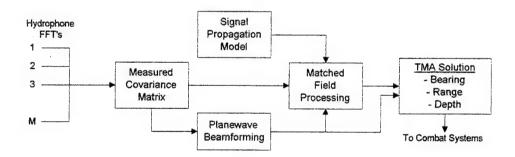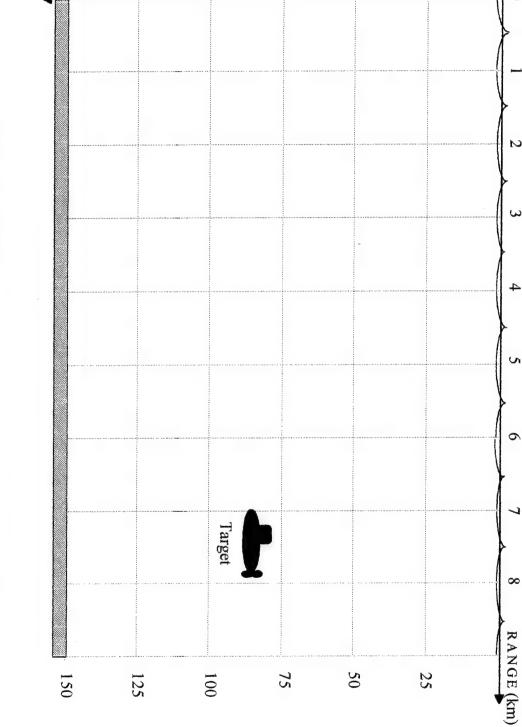
Figure 3.1 MFP block diagram.

wave beamforming is performed in conjunction with MFP. The target location is resolved by correlating the measured hydrophone outputs to a series of predicted values at several different range/depth cells (see Fig. 3.2). The correlation coefficient (or beamformer output) is calculated for each cell and plotted on a correlation surface, as shown in Fig. 3.3. A spike in the correlation surface indicates the most probable target location. This method is similar to covariance matrix plane wave beamforming, except that instead of

19

Figure 3.2 Typical range/depth cell grid for shallow water MFP.

DEPTH (m)

RANGE (km)
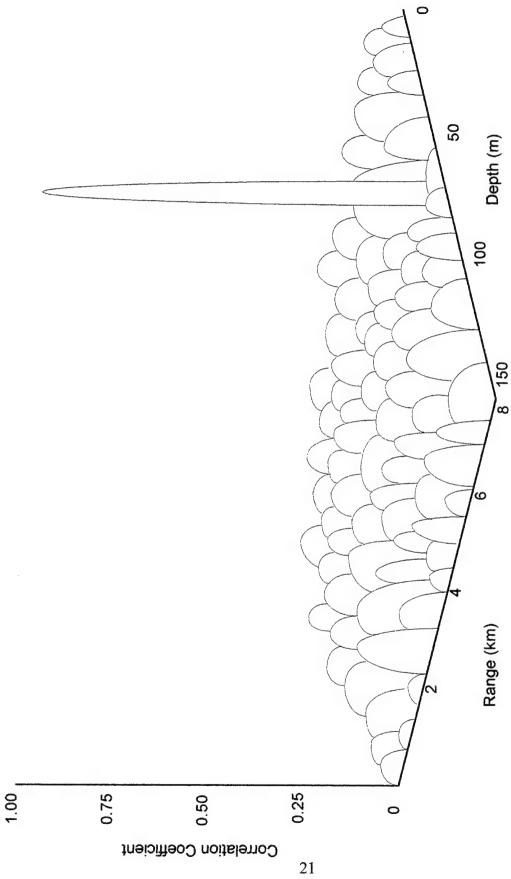
Figure 3.3 Typical correlation surface generated by MFP.

21

using plane wave steering vectors, MFP uses predicted complex pressure vectors obtained from an appropriate propagation model of the environment with an assumed source location. These predicted fields are more realistic than the plane wave fields assumed by conventional beamformers which assume a source at infinite range.

B. IBF/MFP ALGORITHM

1. MFP Beamforming

MFP is actually beamforming in range/depth space instead of frequency/azimuth space associated with plane wave beamforming. The MFP beam pattern (or correlation output) for an equally spaced n element line array is determined by:

$$B(f,R,D,t) = \frac{1}{M^2} [SV'] \cdot [COV(f)] \cdot [SV] \qquad (3.1)$$

where $B(f,R,D,t)$ is the MFP beamformer output as a function of frequency, range, depth and time, and $COV(f)$ is the covariance matrix. The steering vectors are determined from the acoustic propagation model. The correlation output is controlled by the array geometry (which affects the covariance matrix) and the sound propagation environment (which affects the steering vectors and the covariance matrix).

2. Eight Nearest Neighbor Peak Picker (ENNPP)

As correlation coefficients are generated, the output is evaluated for the presence of relative maxima on the correlation surface (see Fig. 3.3). However, location of a true source is sometimes ambiguous, particularly when the signal level is very weak. To

22

overcome this problem, an *Eight Nearest Neighbor Peak Picker* (ENNPP) algorithm [Ref. 24-26] is used to identify relative peaks in the correlation surface. This algorithm, which is illustrated in Fig. 3.4, compares each correlation coefficient with those in the eight adjacent range/depth cells, and defines a "peak" as a correlation coefficient which is greater than all eight of the correlation coefficients in the surrounding range/depth cells. The example in Fig. 3.4 shows a correlation peak located in range/depth cell (2,2).

	Depth 1	Depth 2	Depth 3
Range 1	0.2	0.1	0.2
Range 2	0.1	0.7 Peak	0.3
Range 3	0.4	0.2	0.1

Figure 3.4 Eight nearest neighbor peak picker.

3. M of N Tracker

The *M of N Tracker* [Ref. 24-26] is a three dimensional tracker (beam level vs. range, depth and time) which operates in conjunction with the ENNPP to reduce false target detections. The tracker parameters include range and depth tolerances which establish a neighborhood of range/depth cells within which a correlation peak is allowed to move in a set of N time epochs. If the peak falls within the preset tolerances in "M" of "N" epochs, the successive peaks are considered a target track. There are also range and depth variation fixes which are set "on" (to fix the tolerance in space) or "off" (to allow the tolerance to move with time). Table 3.1 lists the tracker parameters.

Parameter	Setting
• M of N	$M/N \cong 0.67$ with N matched to system averaging time
• Range Tolerance	To be determined
• Range Variation Fix	Normally "off"
• Depth Tolerance	To be determined
• Depth Variation Fix	Normally "on"
• Peak Time Averaging	Usually set to M or less
• Threshold	"On" or "Off"
• Zoom	

Table 3.1 M of N Tracker Parameters and Settings.

The basic operation of the tracker is illustrated in Fig. 3.5. The range tolerance (ΔR) is established at time zero around the first peak validated by the ENNPP. Peaks which appear in successive time epochs are considered as peaks in the track only if they fall within the preset range tolerance. With the range variation fix set "off", the range tolerance moves with each time epoch to center itself around the most recent peak. If two peaks appear within the range tolerance, two separate range tolerances are established in the time epoch, one around each peak, thereby generating two possible tracks. A track is designated as a target only if there are M of N peaks that satisfy the tracker settings. In
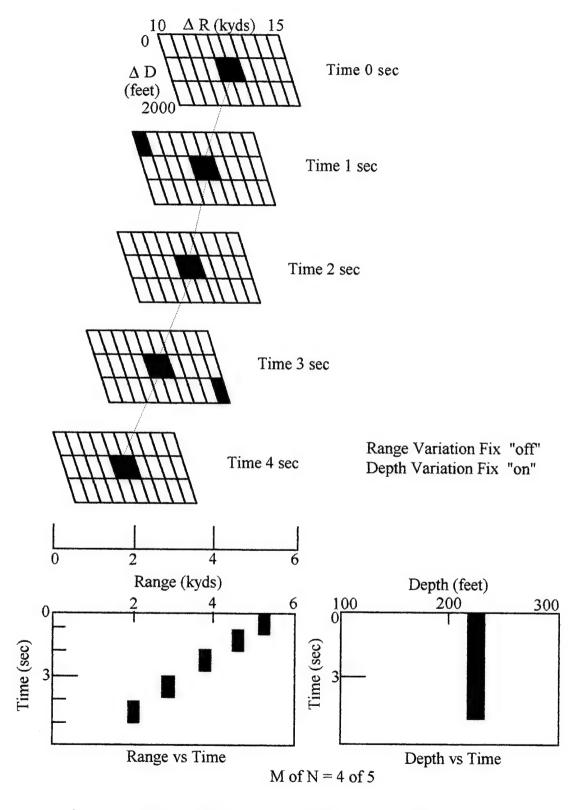
Figure 3.5 M of N tracker and displays.

Fig. 3.5, since M of N is preset to 4 of 5, there must be 4 valid peaks in 5 successive time epochs to generate a track.

While targets are expected to have opening or closing range rates, depth is expected to be constant for significant periods of time. The depth variation fix is therefore set "on" to keep the depth tolerance fixed. In general, the depth vs. time display is used as a classification tool to distinguish submarines from surface ships, and to alert the tracking party to a change in depth by the target vessel.

The *threshold* setting is available to further reduce false target detections. When it is set "on", peak values which fall below the preset correlation threshold are ignored by the tracker. The threshold level is determined by the operator based on the correlation characteristics of the acoustic environment.

Gray shading provides video enhancement to distinguish between "strong" and "weak" targets. Normally, tracks with high correlation values are displayed as bright white, while tracks with very low correlation values are displayed as dark gray. Color enhancement is also available to aid the operator in identifying the depth of any particular range track. For example, range tracks may be designated as blue to indicate surface tracks, red to indicate submerged tracks from 100 to 300 feet in depth, yellow to indicate 300 to 500 feet, etc.

V. ACOUSTIC PROPAGATION MODELS

The complex steering vectors used in MFP must be calculated using an acoustic model which takes into account the propagation characteristics of the waveguide (i.e., normal mode model for shallow water and/or low frequency signals, and ray theory for high frequency signals in deep water). One possible approach is to use a ray model (such as GSM or CASS) which assumes the source to be stationary during the time period over which each FFT is calculated. However, the preferred method is one which utilizes normal mode concepts [Ref. 32, 33] to predict steering vectors assuming a moving source. Such a method was recently developed to determine the acoustic field of a moving source in a range independent environment [Ref. 34] and will be summarized in this section. This theory has also been extended to estimate the acoustic field from an arbitrary moving source in a range dependent environment [Ref. 35]. For the case of a slowly moving source in the horizontal plane, these results reduce to the well known equation derived by Hawker [Ref. 36]. Although the data analysis performed in this thesis is for a deep water site with a slowly moving source, the theory can be extended to shallow water for a source moving with arbitrary speed.

A. NORMAL MODE MODEL

1. General Solution for a Range-Independent Waveguide

Starting with an idealized, symmetric, range-independent acoustic waveguide with sinusoidal time dependence, acoustic propagation is governed by the reduced wave equation (or Helmholtz equation):

$$\frac{1}{r}\frac{\partial}{\partial r}\left(r\frac{\partial p}{\partial r}\right) + \rho(z)\frac{\partial}{\partial z}\left(\frac{1}{\rho(z)}\frac{\partial p}{\partial z}\right) + \frac{\omega^2}{c^2(z)}p(r,z) = \frac{-\delta(z-z_s)\delta(r)}{2\pi r} \qquad (4.1)$$

where "p(r,z)" is the acoustic pressure at range "r" and depth "z", "$\rho(z)$" is the water density as a function of depth, "c(z)" is the sound speed as a function of depth, and "ω" is the acoustic frequency in rad/sec. Using the technique of separation of variables, the pressure field p(r,z) may be expressed as:

$$p(r,z) = Z(z)R(r) \qquad (4.2)$$

and substituted into Eq. 4.1. This leads to the following equation:

$$\frac{1}{R}\left[\frac{1}{r}\frac{d}{dr}\left(r\frac{dR}{dr}\right)\right] + \frac{1}{Z}\left[\rho(z)\frac{d}{dz}\left(\frac{1}{\rho(z)}\frac{dZ}{dz}\right)\right] + \frac{\omega^2}{c^2(z)} = 0 \qquad (4.3)$$

Since the first term is a function of r only and the second term is a function of z only, the equality is satisfied if and only if both terms are equal to the same constant. If κ^2 is used to represent this constant, then Eq. 4.3 can be rewritten as:

$$-\frac{1}{R}\left(\frac{d^2R}{dr^2} - \frac{1}{r}\frac{dR}{dr}\right) = \frac{1}{Z}\left(\frac{d^2Z}{dz^2} - \frac{1}{\rho(z)}\frac{d\rho}{dz}\frac{dZ}{dz}\right) + \frac{\omega^2}{c^2(z)} = \kappa^2 \qquad (4.4)$$

and the modal equation (or depth equation) becomes:

28

$$\frac{d^2Z}{dz^2} - \frac{1}{\rho(z)}\frac{d\rho}{dz}\frac{dZ}{dz} + \left(\frac{\omega^2}{c^2(z)} - \kappa^2\right)Z = 0. \tag{4.5}$$

Assuming that the ocean surface is a pressure release surface and that the bottom (at depth D) is perfectly rigid, the boundary conditions are:

$$Z(0) = 0, \qquad \frac{dZ(D)}{dz} = 0. \tag{4.6}$$

This is a Sturm-Liouville eigenvalue problem for which there exists an infinite number of solutions (normal modes) characterized by mode shape functions $Z_m(z)$ and horizontal propagation constants κ_m. The propagation constants are distinct eigenvalues and the mode shape functions are the corresponding eigenfunctions. Since these eigenfunctions form an orthonormal set, the term *normal modes* is generally used. The subscript, m, designates the mode number for the particular eigenvalue or eigenfunction.

The pressure field in Eq. 4.2 can now be expressed as:

$$p(r,z) = \sum_{m=1}^{\infty} R_m(r)Z_m(z). \tag{4.7}$$

Substituting this expression into Eq. 4.1 yields:

$$\sum_{m=1}^{\infty}\left[\frac{1}{r}\frac{d}{dr}\left(r\frac{dR_m}{dr}\right)Z_m + \kappa^2 R_m Z_m\right] = \frac{-\delta(r)\delta(z-z_s)}{2\pi r} \tag{4.8}$$

Equation 4.8 can be simplified by multiplying both sides of the equation by:

$$\int_0^D \frac{Z_l(z)}{\rho(z)} dz \qquad (4.9)$$

and applying the orthogonality property:

$$\int_0^D \frac{Z_m(z)Z_l(z)}{\rho(z)} dz = \begin{array}{l} 0 \ \textit{for } l \neq m \\ 1 \ \textit{for } l = m \end{array} \qquad (4.10)$$

to yield the following equation:

$$\frac{1}{r}\frac{d}{dr}\left(r\frac{dR_l}{dr}\right) + \kappa_l^2 R_l = \frac{-\delta(r)Z_l(z_s)}{2\pi r \rho(z_s)}. \qquad (4.11)$$

The solution to Eq. 4.11 is a Hankel function of the first kind:

$$R_l(r) = \frac{i}{4\rho(z_s)} Z_l(z_s) H_0^{(1)}(\kappa_l r) \qquad (4.12)$$

where the asymptotic approximation of the Hankel function is:

$$H_0^{(1)}(\kappa_m r) \approx \sqrt{\frac{2}{\pi \kappa_m r}} \, e^{i(\kappa_m r - \frac{\pi}{4})}. \qquad (4.13)$$

The full normal mode solution for the pressure field can now be written as:

$$p(r,z) = \frac{i}{4\rho(z_s)} \sum_{m=1}^{\infty} Z_m(z_s)Z_m(z)H_0^{(1)}(\kappa_m r) \qquad (4.14)$$

or substituting the asymptotic approximation in Eq. 4.13:

$$p(r,z) \approx \frac{i}{\rho(z_s)\sqrt{8\pi r}} e^{-i\pi/4} \sum_{m=1}^{\infty} Z_m(z_s) Z_m(z) \frac{e^{i\kappa_m r}}{\sqrt{\kappa_m}}. \tag{4.15}$$

The complete, time-dependent solution for the pressure field is:

$$P(r,z,t) = p(r,z)\, e^{-i\omega t} \tag{4.16}$$

or

$$P(r,z,t) \approx \frac{i}{\rho(z_s)\sqrt{8\pi r}} e^{-i(\omega t + \pi/4)} \sum_{m=1}^{\infty} Z_m(z_s) Z_m(z) \frac{e^{i\kappa_m r}}{\sqrt{\kappa_m}}. \tag{4.17}$$

2. The Isospeed Problem

A specific analytical normal mode solution can be obtained by assuming that the sound speed c and the density ρ in the water column are constant. Under these conditions, the general solution for the normal mode functions becomes:

$$Z_m(z) = A \sin\gamma z + B \cos\gamma z, \tag{4.18}$$

where

$$\gamma = \sqrt{\frac{\omega^2}{c^2} - \kappa^2}. \tag{4.19}$$

The boundary conditions specified in Eq. 4.6 lead to the condition:

$$A \cos\gamma D = 0 \tag{4.20}$$

31

where D is the bottom depth. The non-trivial solution is therefore:

$$\gamma D = (m + \tfrac{1}{2})\pi, \quad m = 1, 2, ..., \tag{4.21}$$

with the eigenvalues, or normal wave numbers, assuming the discrete values:

$$\kappa_m = \sqrt{\frac{\omega^2}{c^2} - \left[\left(m + \frac{1}{2}\right)\frac{\pi}{D}\right]^2} \qquad m = 1, 2, ... \tag{4.22}$$

and with the corresponding eigenfunctions, or normal modes, given by:

$$Z_m(z) = \sqrt{\frac{2}{D}} \sin \gamma_m z. \tag{4.23}$$

Substituting Eq. 4.21 into Eq. 4.14, the complex pressure field becomes:

$$p(r,z) = \frac{i}{2D} \sum_{m=1}^{\infty} \sin(\gamma_m z_s) \sin(\gamma_m z) H_0^{(1)}(\kappa_m r). \tag{4.24}$$

Since the eigenvalues (κ_m) must be real valued for their associated modes to propagate, only a finite number of modes will exist in any given waveguide. For shallow water, the normal mode expansion is very efficient and only a few modes are required. In deep water, as in RANGEX 1-92, many more modes are required and the normal mode expansion is not efficient. However, the ray theory approximation generally holds true

for most deep water environments, allowing for the use of a ray model in deep water, which is much more efficient than a normal mode model.

To illustrate the effect of the waveguide on normal mode propagation, consider a low frequency tonal (26 Hz) in a waveguide similar to the RANGEX 1-92 area (4000 m water depth) with $c = 1500$ m/sec. Substituting these values into Eq. 4.22 yields:

$$\kappa_m = \sqrt{\frac{(2\pi \cdot 26Hz)^2}{(1500m/\sec)^2} - \left[(m+1/2)\frac{\pi}{4000m}\right]^2}$$

$$= \sqrt{(0.1089\,m^{-1})^2 - [0.000785398\,m^{-1}(m+1/2)]^2} \ .$$

For κ_m to be real valued, the quantity inside the radical must be positive. This requires that the second term inside the radical be less than the first term:

$$0.000785398(m + \tfrac{1}{2}) \ \leq \ 0.1089$$

or $\qquad\qquad m \ \leq \ 0.1089/0.000785398 - \tfrac{1}{2} \ \approx \ 138.$

For values of $m > 138$, the eigenvalues are imaginary and the exponential portion of the Hankel function (Eq. 4.13) becomes:

$$e^{i(\kappa_m r - \pi/4)} \ = \ e^{i(i|\kappa_m|r - \pi/4)} \ = \ e^{(-|\kappa_m|r - i\pi/4)} \qquad \text{where } \kappa_m = i|\kappa_m|.$$

The pressure field (Eq. 4.15) for the case of imaginary eigenvalues is therefore:

$$p(r,z) \ \approx \ \frac{ie^{-i\pi/4}}{\rho(z_s)\sqrt{8\pi r}} \sum_{m=1}^{\infty} Z_m(z_s)Z_m(z)\frac{e^{-|\kappa_m|r}}{\sqrt{i|\kappa_m|}} \ .$$

33

Since the exponential function inside the summation is now a decay function, all modes corresponding to m > 138 will decay exponentially. For a shallow water environment (e.g., D = 100 meters), only the first two modes would propagate; the rest would decay exponentially.

B. SOLUTION FOR THE ACOUSTIC FIELD OF A MOVING SOURCE

1. Contemporary and Retarded Times in Acoustics

The acoustic field for a slowly moving point source with constant velocity was originally derived 15 years ago by Hawker [Ref. 36]. This solution is given in *contemporary time*, which is the time at which the sound reaches the receiver. However, difficult analytical problems arise when Hawker's approach is extended for the acoustic field of a source with arbitrary velocity. It is useful, therefore, to express the field in retarded time, which is the time at which the energy is radiated by the source. The relationship between retarded time and contemporary time is illustrated in Fig. 4.1. The vectors **r** and **r'** are the position vectors for the source at contemporary time, t, and

Source position
at t'

$$R = r - r'$$
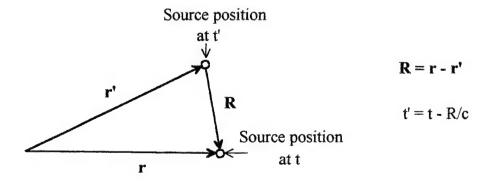
$$t' = t - R/c$$

Source position
at t

**Figure 4.1 Relationship between retarded time (t')
and contemporary time (t).**

34

retarded time, t', respectively. Assuming a constant sound speed, c, the relationship between the retarded and contemporary times is given by the expression:

$$t' = t - R/c \qquad \text{where } R = |\mathbf{r} - \mathbf{r}'|. \tag{4.25}$$

2. Acoustic Field Solutions

The solution for the acoustic field of a source with an arbitrary velocity and frequency ω_0 in a range independent environment was recently developed by Lim and Ozard (1994a). This solution, expressed in retarded time, is given by:

$$P(r,z,t) = -\frac{1}{8\pi\rho} \sum_{m=1}^{\infty} \int_{-\infty}^{+\infty} e^{-i\omega_0 t'} dt' \int_{-\infty}^{+\infty} \frac{Z_n(z)Z_n(z_s)}{(\omega - \omega_0)} e^{-i\omega(t-t')} \frac{dH_0(\kappa_m^0 r)}{dt'} d\omega. \tag{4.26}$$

For the case of a slowly moving source, Eq. 4.26 simplifies to:

$$P(r,z,t) \approx \frac{i}{\rho(z_s)\sqrt{8\pi r(t')}} e^{-i(\omega_0 t + \pi/4)} \sum_{m=1}^{\infty} Z_m^0(z_s)Z_m^0(z)\frac{e^{i\kappa_m^0 r(t')}}{\sqrt{\kappa_m^0}} \tag{4.27}$$

where $t' = t - r(t')/c_m$ is the retarded time, c_m is the modal group speed, and where the superscript "0" indicates functions evaluated at the source frequency, ω_0. Note that Eq. 4.27 is similar to the normal mode solution given in Eq. 4.17, except that the position, r, is specified as a function of retarded time, t'.

Consider now the special case of a slow-moving source with constant horizontal velocity, as in Hawker's model. Define the angle, α, as:

$$\sin \alpha(t) \equiv -\hat{v} \cdot \hat{r}(t) \tag{4.28}$$

35

where $\hat{v}(t)$ is the unit vector in the direction of target motion, and $\hat{r}(t)$ is the unit vector from the source to the receiver at time t. The expression for r(t') now becomes:

$$r(t') \approx r(t)\left[1 - \frac{v \sin \alpha(t)}{c_m}\right] \tag{4.29}$$

where v is the speed of the source. The term $v \sin \alpha(t)$ gives the velocity component in the line of sight and corrects for the pressure wave phase shift for a moving target. Equation 4.29 can be substituted into Eq. 4.27 to obtain the acoustic field in contemporary time:

$$P(r,z,t) \approx \frac{i}{\rho(z_s)\sqrt{8\pi r(t)}}e^{-i(\omega_0 t+\pi/4)}\sum_{m=1}^{\infty}\frac{Z_m^0(z_s)Z_m^0(z)}{\sqrt{\kappa_m^0}}e^{i\kappa_m^0 r(t)[1-(v/c_m)\sin \alpha(t)]} \tag{4.30}$$

This is Hawker's solution [Ref. 36] for the acoustic field of a slowly moving source with constant velocity. This solution will be utilized for calculation of steering vectors, as described in the next section.

Although the previous discussion of normal mode theory was limited to range independent environments, Lim and Ozard [Ref. 35] have extended the calculations to sources moving in *weakly* range-dependent environments (i.e., environments in which the sound speed and bathymetry are weak functions of the horizontal displacement). Even though the solutions for the acoustic field in cases of arbitrary range dependence are unknown, the equations can be solved for some specific ocean geometries. In addition, Lim and Ozard developed a perturbation approach to provide a reasonably accurate

36

model of sound propagation over the continental shelf. The mathematical details for these cases will not be discussed in this thesis.

C. CALCULATION OF STEERING VECTORS

The steering vectors used for MFP in shallow water are determined using Eq. 4.30 to predict the acoustic pressure at each hydrophone location with the acoustic source at an assumed position. From the law of cosines, the range from the assumed source location to the nth hydrophone, $r_n(t)$, is given by:

$$r_n(t) = \{r^2(t) + [(24.5 - n)d]^2 + r(t)[24.5 - n]d\cos\theta_r\}^{1/2} \tag{4.31}$$

where $r(t)$ is the range from the predicted source location to the center of the array, θ_r is the relative bearing to the source, d is the hydrophone spacing, and n is the hydrophone number (1 to 48). For each range/depth cell (see Fig. 3.2), the acoustic pressure at the nth hydrophone can be calculated using Eq. 4.30:

$$P_n(r_n, z, z_s, t) \approx \frac{i}{\rho(z_s)\sqrt{8\pi r_n(t)}} e^{-i(\omega_0 t + \pi/4)} \sum_{m=1}^{\infty} \frac{Z_m^0(z_s)Z_m^0(z)}{\sqrt{\kappa_m^0}} e^{i\kappa_m^0 r_n(t)[1 - (v/c_m)\sin\alpha(t)]}$$

where the each value of $r_n(t)$ is calculated from Eq. 4.31, and the normal mode values (Z_m) are determined from the SACLANTCEN Normal Mode Acoustic Propagation Model (SNAP) [Ref. 37] based on inputs of $c(z)$ and water depth (see Appendix B). The

velocity of the source is assumed to be zero initially, and then updated when range rate estimates are obtained from the MFP alogorithm. For the 48 element line array used to obtain the data in this thesis, the steering vector for each range/depth cell is given by:

$$
SV = \begin{bmatrix} P_1(r_1, z, z_s, t) \\ P_2(r_2, z, z_s, t) \\ \vdots \\ P_{48}(r_{48}, z, z_s, t) \end{bmatrix}.
\tag{4.32}
$$

Note that the variables r and z_s represent the range and depth, respectively, of each range/depth cell. Each value of r is applied to Eq. 4.31 to calculate the variable r_n, which, along with the values of z_s, are used to determine the acoustic pressures at the hydrophones.

D. CASS SUMMARY

In some cases, it may be preferred to calculate the acoustic pressures using a ray model such as CASS [Ref. 38]. In deep water, for example, CASS is much more efficient than the normal mode model which requires calculations of hundreds of mode functions for each range/depth cell. However, it is important to remember that CASS assumes the target to be stationary between FFT intervals. This may be of no consequence when dealing with slow moving targets, but could be a significant source of error for faster targets such as torpedoes. The selection of the appropriate acoustic propagation model must therefore be based on the tradeoff of efficiency in calculations versus the accuracy of the model.

38

1. Basic Description

CASS is a ray model developed for determining acoustic propagation primarily in deep water. To use CASS for MFP tracking of a moving source, the following assumptions must be made:

a. the environment is range independent, and

b. the acoustic source does not move a significant distance in one averaging time (i.e., slow moving target).

The principle advantage of using CASS for MFP is that the eigenrays can be specified by amplitude, conical angle, and relative phase within the CASS model.

2. Calculation of Steering Vectors

As with the normal mode model, steering vectors are determined from the complex pressures provided by the propagation model. Figure 4.2 shows the geometry utilized by CASS in calculting the pressure at each hydrophone.

For any given range/depth cell, the complex pressure is given by:

$$p_m(f) = \sum_{i=1}^{I_{max}} A_i e^{i\left(2\pi\frac{f}{c}|r_m|\cos\psi_i + \Phi_i\right)} \tag{4.33}$$

where A_i is the amplitude, Φ_i is the relative phase, and ϕ_i is the elevation angle of the ith eigenray. The conical angle, Ψ_i is detemined from the relationship

$$\cos\Psi_i = \cos(\theta - H)\cos(\phi_i). \tag{4.34}$$

39
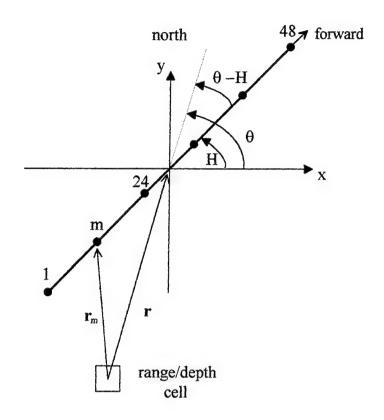
Figure 4.2 Geometry for calculating complex pressures with CASS.

For each eigenray within a user specified portion of the maximum eigenray level (measured by A_i), the values of A_i, ϕ_i and Φ_i are provided by CASS and utilized in Eq. 4.33 to calculate the value of p_m (f). The steering vectors are then determined from Eq. 4.32, and the MFP correlation coefficient is calculated, as before, using Eq. 3.1.

VI. MFP ANALYSIS AND TEST RESULTS

A. INTRODUCTION

In section III.B, it was shown that the MFP beam pattern is determined by Eq. 3.1:

$$B(f,R,D,t) = [SV^t] \cdot [COV(f)] \cdot [SV] / 48^2$$

where the covariance matrix (COV) is measured at the hydrophone outputs, and the steering vector (SV) and its transpose (SV^t) are modeled as a function of range, frequency, source depth, receiver depth and sound speed profile (SSP). Due to the nature of the covariance matrix, the MFP beamformer output (B) can be used to assess complex pressure amplitude and signal coherence simultaneously As Fig. 5.1 shows, the major diagonal terms vary as a function of amplitude only, while the off diagonal terms vary as a function of both amplitude and signal coherence. Since the complex pressure

Figure 5.1 Covariance matrix composition.

amplitudes are determined in part by the TL, the signal covariance matrix contains information on both TL and signal coherence, each of which affect the magnitude of the beamformer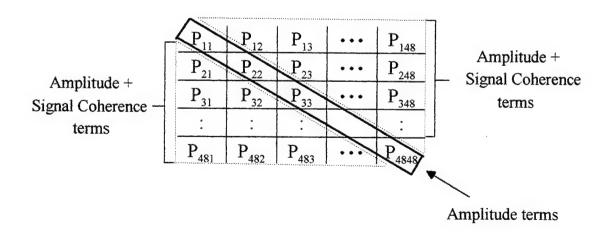 output. The highest beamformer outputs will therefore occur in those cases where the combination of amplitude and signal coherence is highest.

The performance of MFP is tested in the following section using simulated targets to evaluate various test cases in shallow water. The targets are simulated by utilizing Hawker's formula (Eq. 4.30) to calculate the appropriate acoustic pressures at the desired target range and depth, after which a signal covariance matrix is assembled from the calculated pressures. The final section in this chapter evaluates the performance of the MFP algorithm along with the ENNPP and M of N tracker for the RANGEX 1-92 data.

B. SHALLOW WATER TEST CASES

All of the test scenarios were constructed assuming a 48 element horizontal line array with a hydrophone spacing of 1.132 m. Unless otherwise noted, each case assumed a hard, reflective bottom , a constant water depth of 100 m, a source depth of 40 m, a receiver depth of 80 m and a target relative bearing of 45^0. The MFP beamforming algorithm was tested to evaluate the effects of normalization, acoustic frequency, bottom type, SSP, source and receiver depth, and target relative bearing.

1. Normalization Techniques

To effectively evaluate MFP, the MFP beamformer output must be corrected to account for the effects of low transmission loss at close ranges. The impact of TL on the beamforming process is illustrated in Fig. 5.2(a), which shows a typical plot of MFP
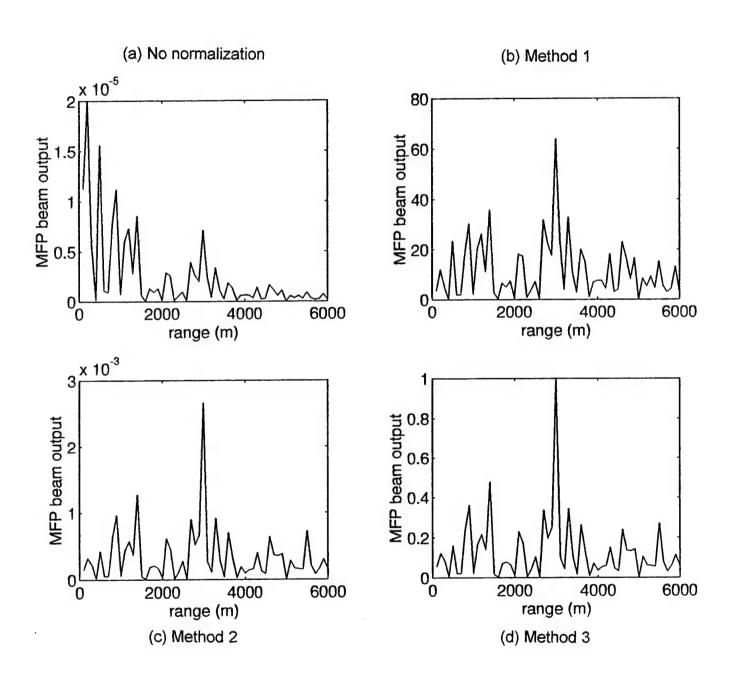
Figure 5.2 Beamformer output vs. range for various normalization techniques.

43

beamformer output versus range (i.e., correlation curve) at 662 Hz. The target for this example has a range of 3000 m. While this curve does show a moderate peak at a range of 3000 m (corresponding to the target), it also shows some larger, secondary peaks (or side lobes) at ranges less than 2000 m. These side lobes, which are undesirable because they "mask" the target, are a result of the cylindrical spreading term in Eq. 4.30 ($1/r^{1/2}$) which causes the steering vectors to have high complex pressure amplitudes at close ranges. To correct the beamformer output for these TL effects, three different methods of normalization were tested. These three methods are illustrated in Fig. 5.2 (b-d) and summarized in the following sections.

a. Method 1

Each steering vector was normalized by removing the cylindrical spreading term from Eq. 4.30, thus removing the contribution of transmission loss to the amplitudes of the predicted pressures. As can be seen in Fig. 5.2(b), this method greatly reduced the side lobes at close ranges while amplifying the relative magnitude of the primary peak corresponding to the target.

b. Method 2

This method was tested as a means of adjusting the scale of the vertical axis such that the beamformer outputs would have values between 0 and 1, thus allowing for a more objective comparison of beamformer outputs at all depths. The steering vectors in this case were normalized by dividing each of the complex pressures by the average magnitude for the entire vector. As Fig. 5.2(c) shows, the scale of the vertical axis did change, but further normalization is still required.

c. Method 3

The scale adjustment which was desired in method 2 was achieved by normalizing the signal covariance matrix in addition to the steering vector normalization of method 2. This yielded the desired output, as shown in Fig. 5.2(d). The primary peak now has a value of 1 (representing perfect correlation), while the side lobes have values between 0 and 1. This is the preferred method of normalization and is used in all of the test cases discussed in the remainder of this chapter.

2. Acoustic Frequency

MFP correlation curves were plotted for acoustic frequencies of 662 Hz, 138 Hz, and 55 Hz as shown in Fig. 5.3, 5.4 and 5.5. Each figure shows a set of four correlation curves with target range initially at 2000 m and moving outward to 5000 m. The 662 Hz curves in Fig. 5.3 each show a clearly defined primary peak corresponding to the target, and much smaller side lobes. The 138 Hz and 55 Hz curves, however, clearly show a progressive increase in the side lobe height with decreasing frequency. This is not surprising, considering that at 55 Hz the acoustic wavelength is 27 m, or twenty four times the hydrophone spacing, while at 662 Hz the acoustic wavelength is 2.26 m, or two times the hydrophone spacing. MFP is clearly most effective at 662 Hz and perhaps marginally effective at 138 Hz. At 55 Hz, the side lobes are so high that it is impossible to distinguish them from the peak.

The effect of acoustic frequency is further illustrated in Fig. 5.6, which shows normalized beam outputs versus target range for the case of plane wave steering vectors. For these curves, a beamformer output close to 1 indicates good correlation between the

45
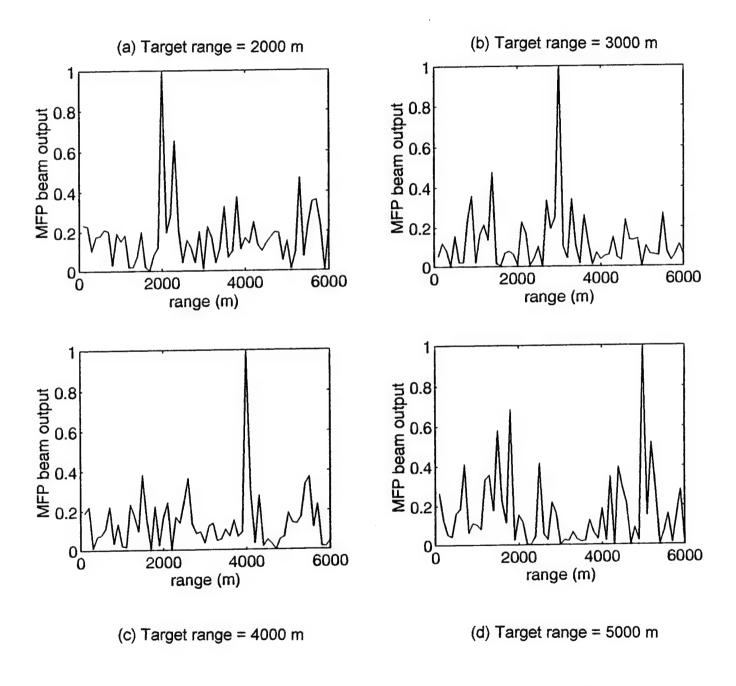
Figure 5.3 Correlation curves for various target ranges at 662 Hz.

(a) Target range = 2000 m

(b) Target range = 3000 m

(c) Target range = 4000 m

(d) Target range = 5000 m
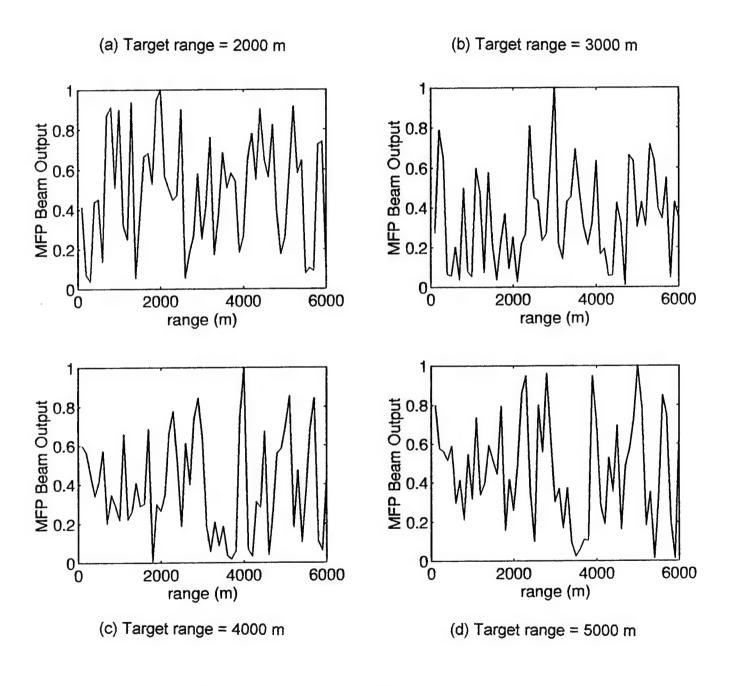
Figure 5.4 Correlation curves for various target ranges at 138 Hz.

(a) Target range = 2000 m

(b) Target range = 3000 m

(c) Target range = 4000 m

(d) Target range = 5000 m
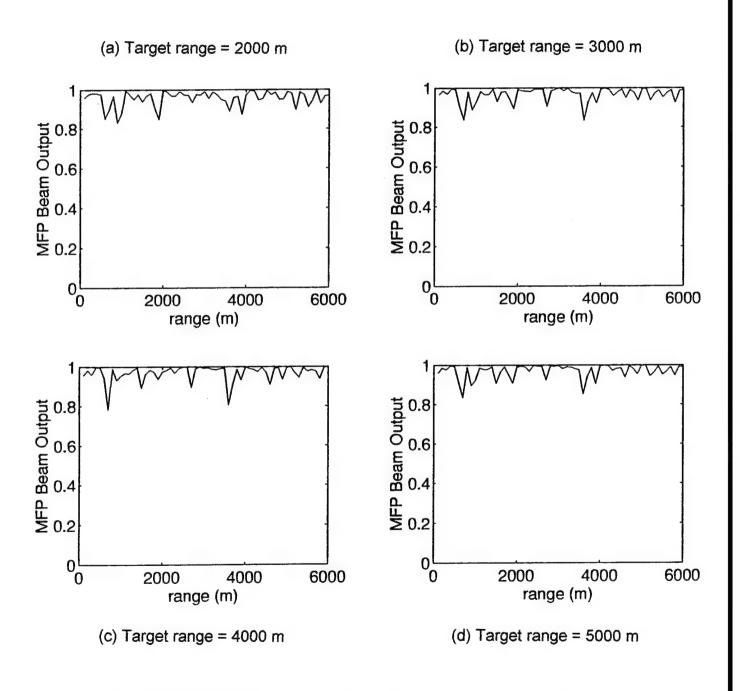
Figure 5.5 Correlation curves for various target ranges at 55 Hz.

* - 662 Hz   o - 138 Hz   x - 55Hz
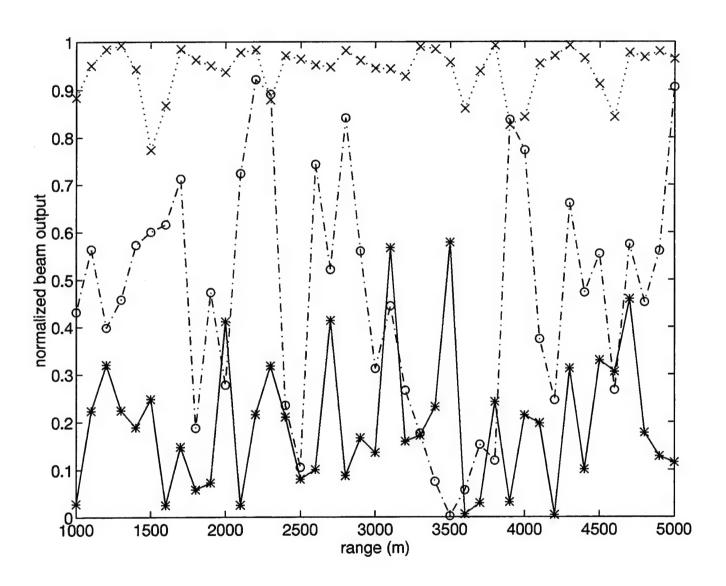
Figure 5.6 Normalized beam output vs. target range
using plane wave steering vectors

signal and the plane wave, while an output close to 0 indicates poor plane wave correlation. As the plot shows, the 55 Hz signals correlate very well with the plane waves, but the 662 Hz signals correlate very poorly. This further explains why the MFP side lobes are so high at 55 Hz, but much smaller at higher frequencies. At 55 Hz, the array "sees" the acoustic signals as plane waves, and is therefore unable to resolve range, since plane wave signal coherence does not vary as a function of range. A plane wave beamformer in this environment would be expected to perform quite well at 55 Hz, but the MFP beamformer would perform poorly at this frequency. At 662 Hz, the situation is reversed. Since the acoustic wavelength is much shorter, the array *is* able to resolve range and it no longer sees the acoustic signals as plane waves. At this frequency, we expect a plane wave beamformer to perform poorly in this environment, while the MFP beamformer would perform quite well.

3. Target Relative Bearing

Figures 5.7 and 5.8 show correlation curves at 662 Hz for target relative bearings ranging from 0^0 (end-fire) to 90^0 (broad side). In Fig. 5.7, the normalized beamformer outputs are calculated using plane wave steering vectors. The plots in this case show that the beamformer outputs are very high (greater than 0.99) at a relative bearing of 90^0, but the values decrease rapidly as the relative bearings get closer to end-fire. A plane wave beamformer should therefore be expected to performer well only if the relative bearing is at or close to broadside. At angles closer to endfire, there is a significant reduction in array gain.

(a) Relative bearing = 0^0

(b) Relative bearing = 30^0

(c) Relative bearing = 60^0

(d) Relative bearing = 90^0

**Figure 5.7 Normalized beam output vs. range at 662 Hz
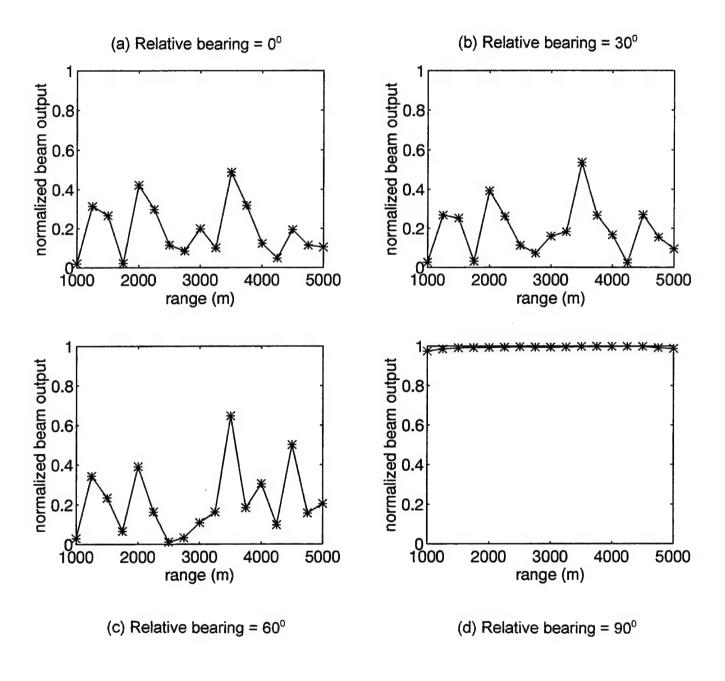for various relative bearings.**
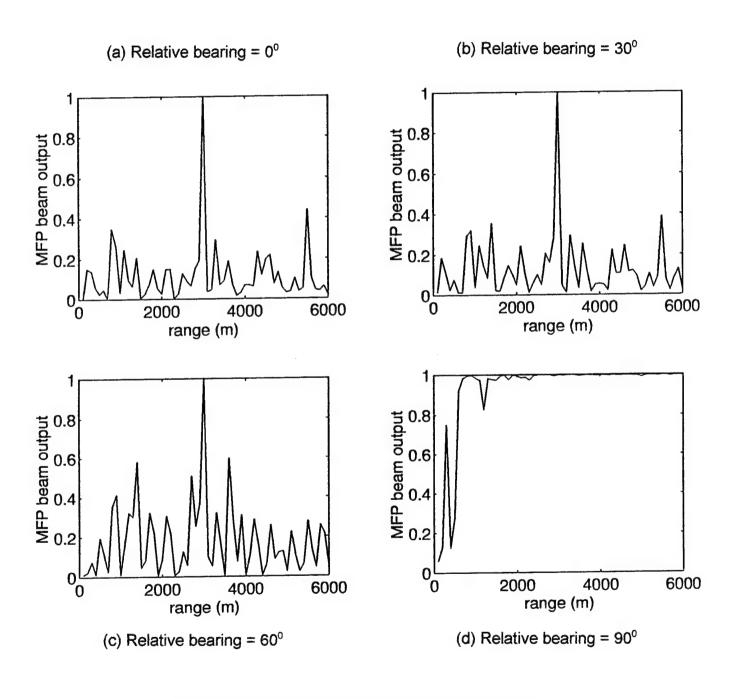
Figure 5.8 MFP beam output vs. range at 662 Hz for various relative bearings.

In Fig. 5.8, MFP beamformer outputs are plotted, again for target relative bearings ranging from end-fire to broad side. These plots clearly show that the MFP beamformer, in contrast to the plane wave beamformer, performs much better at or near end-fire than it does near broadside. For relative bearings at or near broadside, MFP is hardly able to resolve range at all, creating so many side lobes that the correlation curve appears flat. On the other hand, for bearings at or near end-fire, the side lobes are greatly reduced.

4. Bottom Type

Figures 5.9 - 5.11 show the contrast between a hard, reflective bottom type and a softer bottom which absorbs much more acoustic energy. The MFP plots of Fig. 5.9 and 5.10 illustrate that for the same frequency, the side lobes are significantly larger for the soft bottom plots than they are for the hard bottom plots. This is because the softer bottom type "strips" away some of the higher modes in the shallow water wave guide, thereby reducing the uniqueness of the modal interactions at various ranges and causing the larger range/depth side lobes. In the hard bottom cases, a greater amount of acoustic energy is reflected back into the wave-guide, causing a more unique nodal interference pattern with range and thereby reducing the side lobe height.

The effect of acoustic energy absorption by the bottom is further illustrated in Fig. 5.11, which shows normalized beam outputs at 662 Hz using plane wave steering vectors. As expected, the soft bottom plot shows higher values of beam output on the average than the hard bottom plot, indicating that the acoustic signals in the soft bottom environment are more "plane wave" in nature. Again, this is due to modal "stripping" by

(a) Hard bottom, target range 2000 m

(b) Hard bottom, target range 2000 m

(c)Soft bottom, target range 2000 m

(d) Soft bottom, target range 4000 m
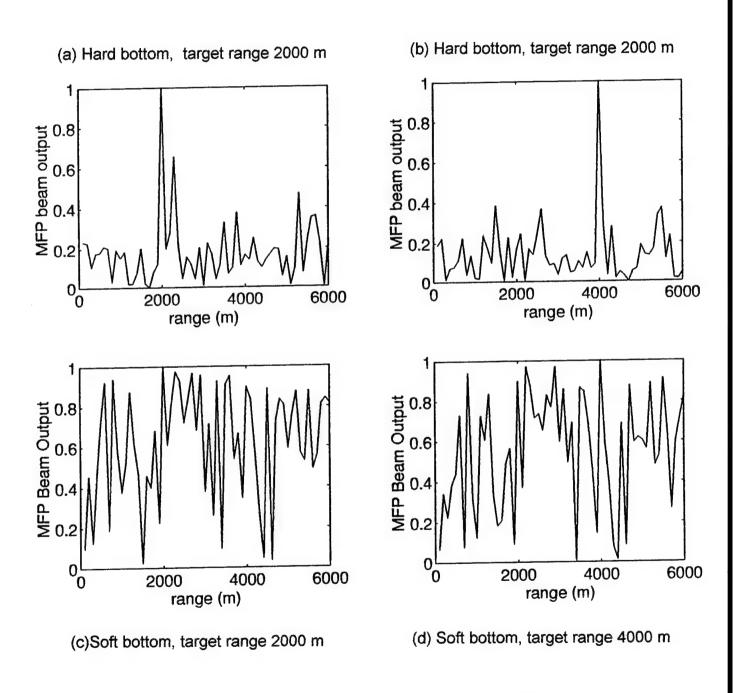
**Figure 5.9 MFP beam output vs. range at 662 Hz
for hard and soft bottom.**

(a) Hard bottom, target range 2000 m

(b) Hard bottom, target range 2000 m

(c) Soft bottom, target range 2000 m

(d) Soft bottom, target range 4000 m
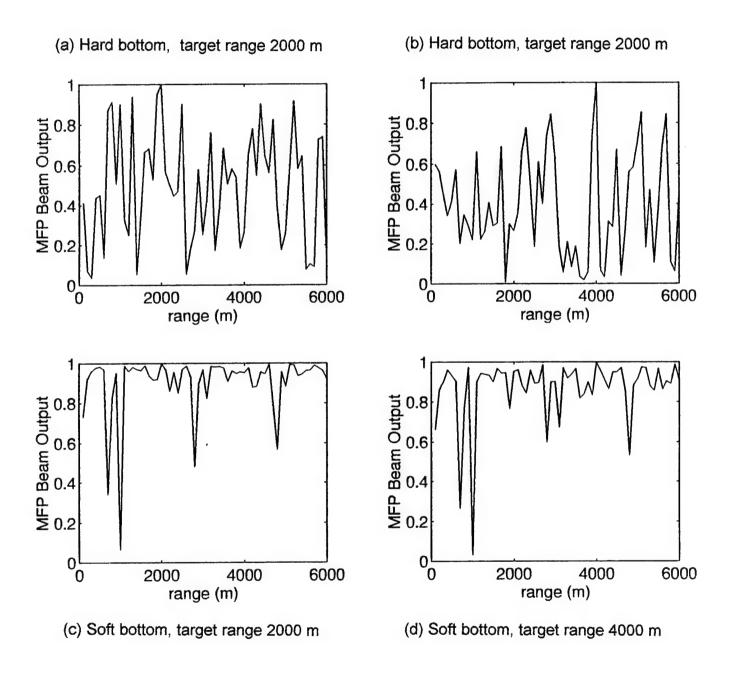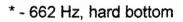
**Figure 5.10 MFP beam output vs. range at 138 Hz
for hard and soft bottom.**
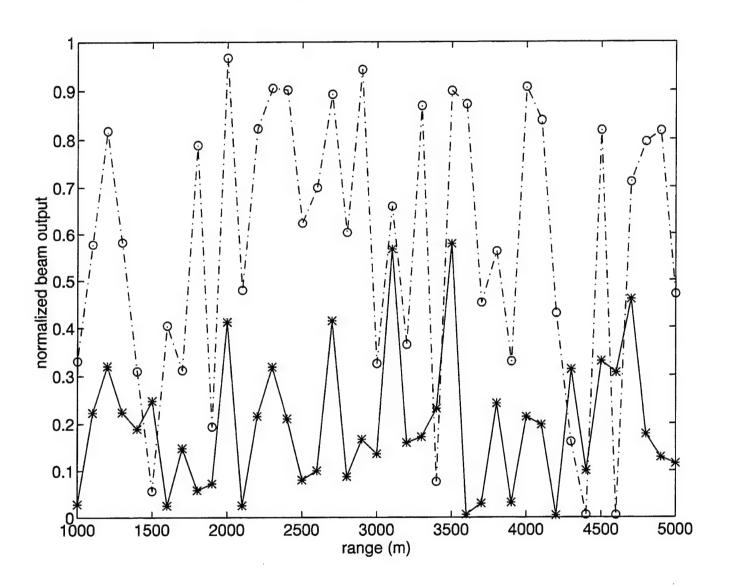
Figure 5.11 Normalized beam output vs. target range using plane wave steering vectors with hard and soft bottom.

the soft bottom which reduces the uniqueness of the modal interactions and causes the acoustic signals to have characteristics more like plane waves.

It should be emphasized that the geoacoustic bottom properties of real ocean environments would generally lie between the two extremes discussed above. However, in those areas where there is significant variability in geoacoustic bottom properties, passive sonar performance may vary noticeably. Specifically, an MFP beamformer would be expected to perform better in hard bottom rather than soft bottom environments, while a plane wave beamformer would be expected to perform better where the bottom is less reflective. It is also noteworthy that at 662 Hz, the plane wave beamformer outputs are, at many ranges, quite low even with a soft bottom, indicating that plane wave beamformer performance in shallow water may be questionable at higher frequencies, regardless of the bottom type.

5. SSP and Source/Receiver Depth

The MFP algorithm was tested for various combinations of source and receiver depth with the SSP's shown in Fig. 5.12. In each case, the acoustic frequency is 662 Hz and the target range is 3000 m. The correlation curves corresponding to each SSP are shown in Fig. 5.13 - 5.16, where four different source/receiver depth combinations are plotted for each SSP. From this series of test cases, the effect of SSP and source and receiver depth on MFP performance is ambiguous. None of the cases show a clear advantage over the other, and there is no discernible relationship between SSP and side lobe height. The results, therefore, are inconclusive, and further testing should be conducted, preferably with real data.

57

Depth (m)	Sound Speed (m/s)
0	1525
20	1518.4
40	1511.8
60	1505.2
80	1498.6
100	1492.0

(a) Week negative gradient
(-0.33 ms^{-1}/m)

Depth (m)	Sound Speed (m/s)
0	1525
20	1515
40	1505
60	1495
80	1485
100	1475

(b) Strong negative gradient
(-0.5 ms^{-1}/m)

Depth (m)	Sound Speed (m/s)
0	1500
20	1506.6
40	1513.2
60	1519.8
80	1526.4
100	1533.0

(c) Weak positive gradient
(+0.33 ms^{-1}/m)

Depth (m)	Sound Speed (m/s)
0	1525
30	1525.5
40	1520.5
60	1513.9
80	1507.3
100	1500.7

(d) Mixed layer

Figure 5.12 Sound speed profiles used for MFP test cases.

D_s - source depth D_r - receiver depth

(a) D_s = 20m, D_r = 80m

(b) D_s = 20m, D_r = 20m

(c) D_s = 50m, D_r = 50m

(d) D_s = 80m, D_r = 80m
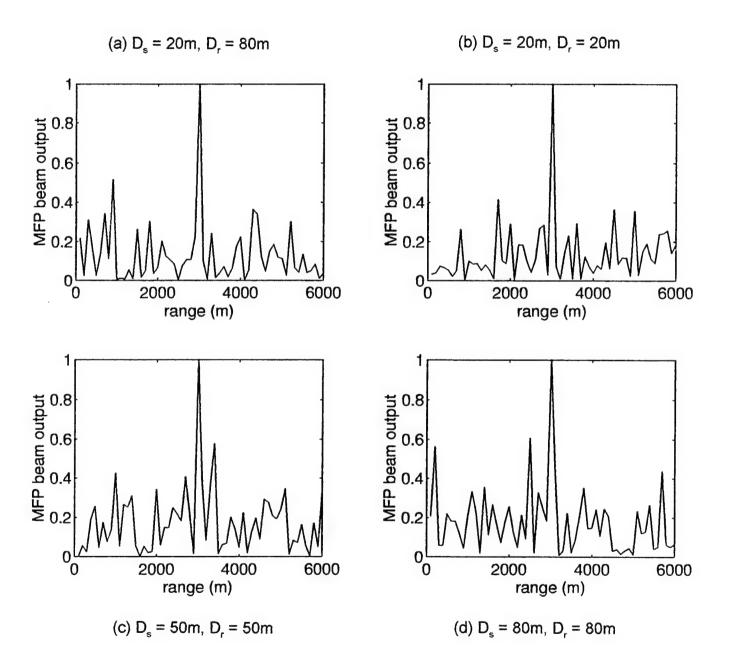
Figure 5.13 MFP beam output vs. range for weak negative gradient.

D_s - source depth D_r - receiver depth

(a) D_s = 20m, D_r = 80m

(b) D_s = 20m, D_r = 20m

(c) D_s = 50m, D_r = 50m

(d) D_s = 80m, D_r = 80m
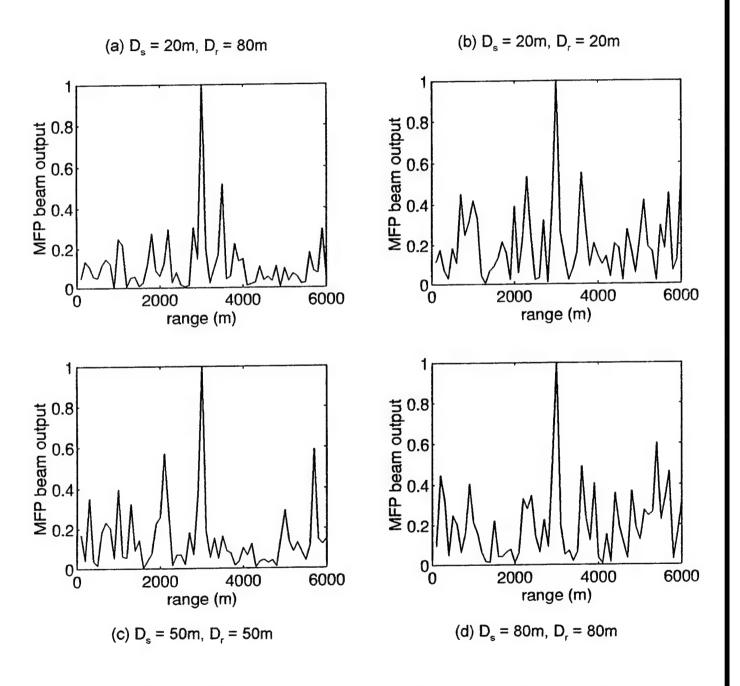
Figure 5.14 MFP beam output vs. range for strong negative gradient.

D_s - source depth D_r - receiver depth

(a) D_s = 20m, D_r = 80m

(b) D_s = 20m, D_r = 20m

(c) D_s = 50m, D_r = 50m

(d) D_s = 80m, D_r = 80m
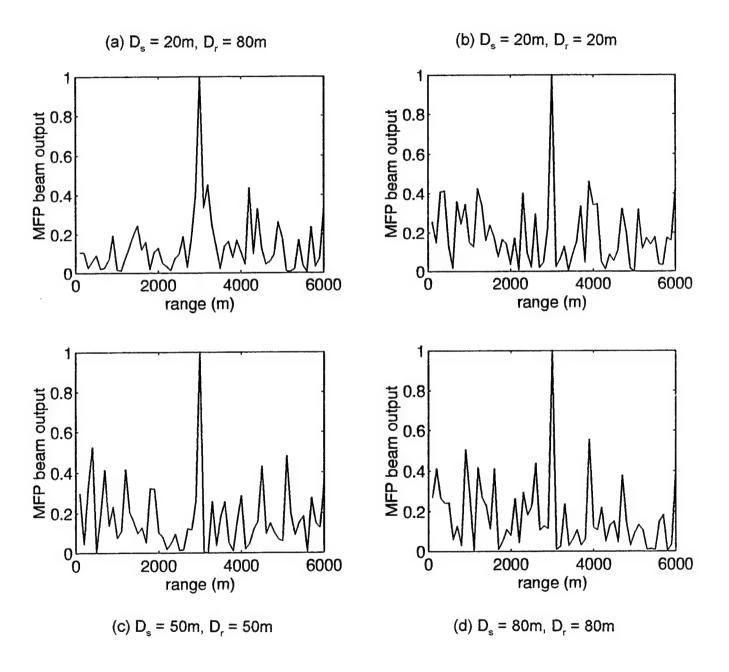
Figure 5.15 MFP beam output vs. range for weak positive gradient.

D_s - source depth D_r - receiver depth

(a) D_s = 20m, D_r = 80m

(b) D_s = 20m, D_r = 20m

(c) D_s = 50m, D_r = 50m
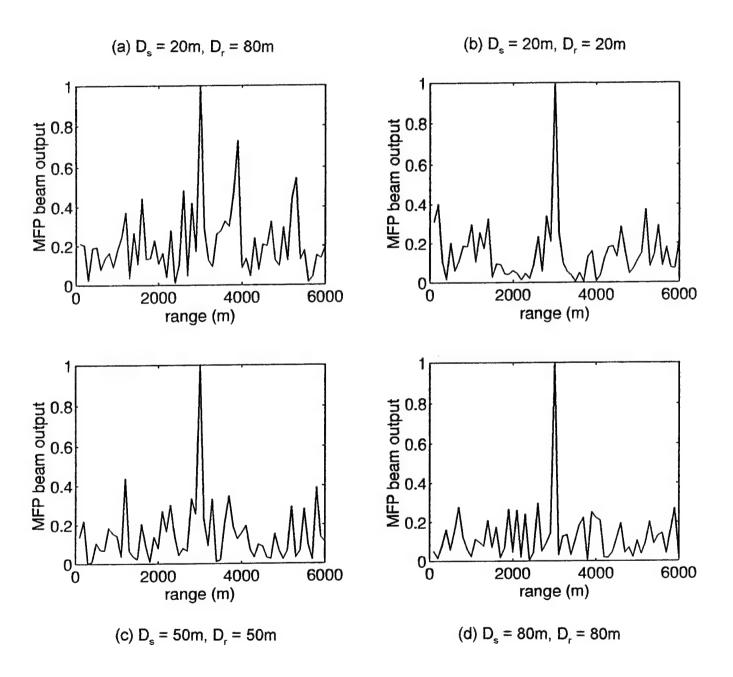
(d) D_s = 80m, D_r = 80m
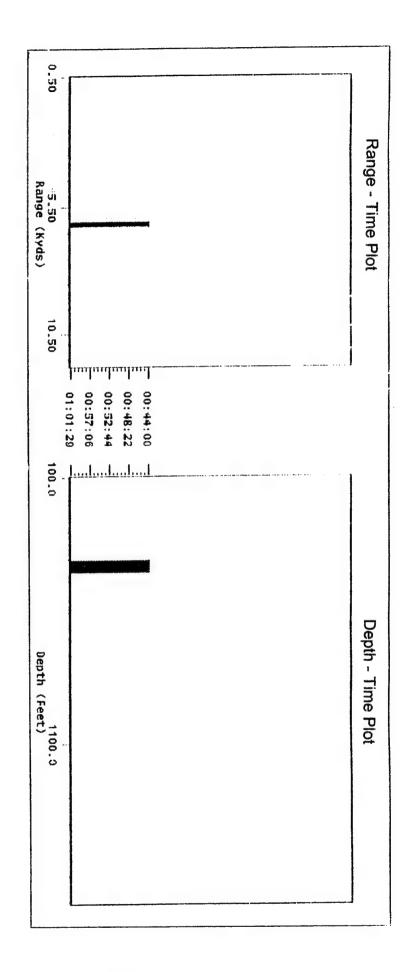
Figure 5.16 MFP beam output vs. range for mixed layer.

C. RANGEX 1-92 ANALYSIS

This deep water data set was utilized to test the operation of the MFP beamforming algorithm along with the ENNPP and M of N tracker in a real ocean environment. Although deep water acoustic propagation differs from shallow water propagation in several respects, this data is nevertheless useful in testing the effectiveness of the ENNPP and M of N tracker in differentiating the actual acoustic source from the side lobes. This is important because as the test cases in the previous section showed, side lobes are a significant problem in MFP beamforming. This real data test will also demonstrate the potential usefulness of the M of N tracker displays for real time shipboard applications.

The ENNPP and M of N tracker were first tested against a simulated target in a deep water environment (water depth 5000 m) with an isospeed profile and utilizing CASS as the acoustic propagation model. The covariance matrix was constructed from acoustic pressures which were calculated from the CASS eigenrays. Figure 5.17 shows the range versus time and depth versus time displays produced by the M of N tracker for a target at a range of 6000 yds and a depth of 400 ft. Note that both plots show a single trace corresponding to the target's range and depth. In this ideal situation, the tracker values correspond exactly to the actual target range and depth, and the operator can easily read the displays in real time.
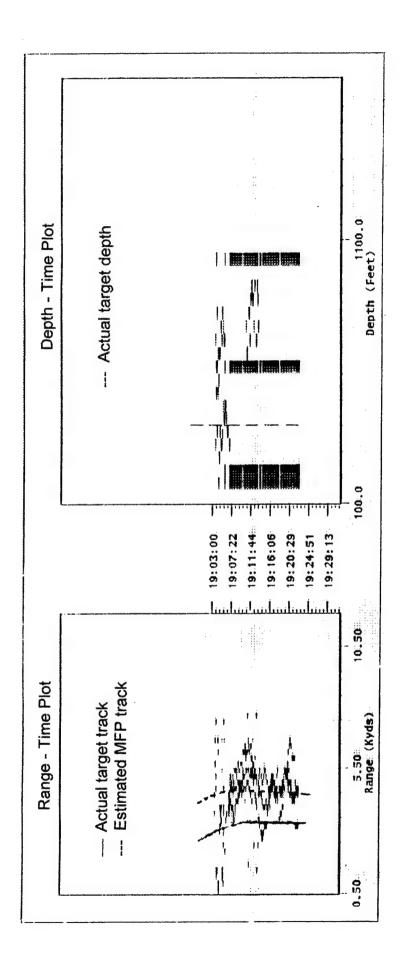
Figure 5.18 shows the tracker displays for a 26 minute portion of data from RANGEX 1-92. This portion of data was selected because the target relative bearing varied by only 3^0, thereby providing for a relatively constant bearing for the calculation

Range - Time Plot

Range (Kyds)

-5.50   5.50   10.50   100.0

00:44:00
00:48:22
00:52:44
00:57:06
01:01:29

Depth - Time Plot

Depth (Feet)

1100.0

Actual target range = 6000 yds   Actual Target Depth = 400 ft

Figure 5.17 M of N tracker displays for a simulated target.

Figure 5.18 M of N tracker displays for RANGEX 1-92 data.

Actual target range ≈ 3000 yds   Actual Target Depth = 400 ft
Estimated MFP range ≈ 4000 yds

of FFT's. Referring first to the range-time display, the actual target track is denoted by the solid line, while the estimated MFP track is denoted by the dotted line. As the plot shows, the MFP track differs from the actual target track by approximately 1000 to 1500 yds. This is an impressive result considering that CASS models the bottom in a very simplistic fashion, treating it as a single layer with a constant speed profile. The range information provided by this display would be very useful in a submarine attack center during a tracking situation, especially considering the fact that range solutions obtained by conventional TMA are seldom within 1000 yds of actual target range. Furthermore, the torpedo firing solutions used in many successful exercise torpedo launches have had range errors of as much as 5000 yds.

The depth estimate, as expected, is not as accurate as the range estimate for this short aperture array, as illustrated by the depth versus time display in Fig. 5.18. While the actual target depth was 400 ft, the tracker shows three traces, none of which are any closer than 200 ft from the actual depth. This demonstrates that for this deep water environment, the MFP beamformer is much better at range discrimination than at depth discrimination. The poor depth discrimination is due to poor vertical sampling by the horizontal line array.

It should be noted that the entire RANGEX 1-92 data set consisted of two hours worth of data, but the majority of the data had high target bearing rates, which are not useful for MFP applications. In general, the bearing rates averaged 3 to 5 ^{0}/min throughout the data set except for that portion which was displayed in Fig 5.18, where the bearing rate was less than 1 ^{0}/min. For bearing rates in excess of 1 to 2 ^{0}/min,

conventional TMA techniques are more useful than MFP. However, the detection and tracking of a slow speed diesel submarine in shallow water, or the tracking of a torpedo before the weapon has reached its enable point are two low bearing rate examples where MFP shows great potential. Certainly, shallow water environments will limit TMA maneuvers significantly and single heading TMA with a towed array is highly desirable.

VII. CONCLUSIONS AND RECOMMENDATIONS

A. CONCLUSIONS

1. Plane wave beamforming with horizontal line arrays may be significantly degraded for relative bearings other than broadside by the multipath/multimode acoustic environment of shallow water, particularly at higher frequencies. Degradation is even greater in those environments with a hard, reflective bottom.

2. MFP performance for horizontal line arrays is significantly affected by:

   - the choice of normalization technique.

   - the geoacoustic properties of the bottom/subbottom.

   - the acoustic frequency.

3. Range/depth side lobes are a significant problem for short horizontal arrays at low frequencies.

4. The IBF ENNPP and M of N tracker show great potential for reducing the impact of range/depth side lobes.

5. MFP with horizontal line arrays shows potential as a means of single heading TMA for submarines operating in shallow water.

B. RECOMMENDATIONS

1. Environmental inputs are very important to the success of MFP. Therefore, greater attention must be given to modeling the environment, especially geoacoustic properties, in potential shallow water areas of interest.

2. Horizontal line array data sets are required in shallow water to conduct further tests of the MFP algorithm.

3. Integrated plane wave - MFP beamformers should be considered for use in shallow water to cover all frequencies of interest.
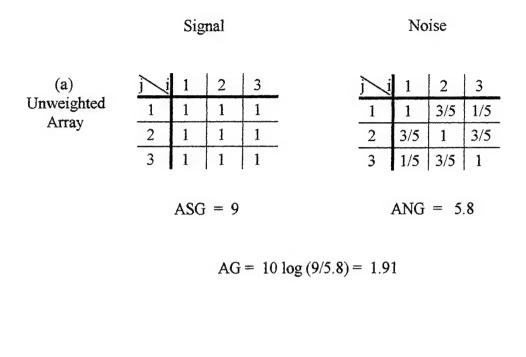
APPENDIX A. FIM DESCRIPTION

The Fourier Integral Method (FIM) [Ref. 27-29] is a beamforming method which improves the array gain for a line array by weighting the cross sensor pairs as a function of the spacing between hydrophones, where the elements with the greatest separation are given the greatest weighting. The method is illustrated in Fig. A.1 for a 3 element, equally spaced line array. The 3 x 3 signal and noise matrices with CBF are constructed from the cross-correlation coefficients of each possible pairing of array elements. The array gain (AG) is given by

$$AG = \frac{ASG}{ANG} \qquad (A.1)$$

where ASG (array signal gain) and ANG (array noise gain) are obtained by summing the elements in the appropriate matrix.

For the matrices shown in Fig. A.1(b), the FIM AG enhancement is the result of dividing each correlation value by the number of elements in the respective diagonal or off diagonal of the matrix. This gives greater weighting to those pairs with the greatest separation, thus improving the array gain. The price that is paid for this AG enhancement is higher peak side lobe levels; however, the IBF post processing algorithms (ENNPP and 3 dimensional M of N tracker) compensate for the higher side lobes.

Signal   Noise

(a)
Unweighted
Array

j \ i	1	2	3
1	1	1	1
2	1	1	1
3	1	1	1

j \ i	1	2	3
1	1	3/5	1/5
2	3/5	1	3/5
3	1/5	3/5	1

ASG = 9   ANG = 5.8

$$AG = 10 \log (9/5.8) = 1.91$$

Signal   Noise

(b)
Weighted
Array
(FIM)

j \ i	1	2	3
1	1/3	1/2	1
2	1/2	1/3	1/2
3	1	1/2	1/3

j \ i	1	2	3
1	1/3	3/10	1/5
2	3/10	1/3	3/10
3	1/5	3/10	1/3

ASG = 5   ANG = 2.6

$$AG = 10 \log (5/2.6) = 2.84$$

Figure A.1 Comparison of array gains for a three element array with no weighting (a) and FIM (b).

APPENDIX B.   SNAP DESCRIPTION

The SACLANTCEN Normal-Mode Acoustic Propagation Model (SNAP) was developed in 1979 by Finn B. Jensen and Melchiorre C. Ferla of the SACLANT ASW Research Center, San Bartolomeo, Italy [Ref. 37].   It is a normal mode acoustic model intended primarily for a shallow-water ocean environment and designed to provide the outputs shown in Table B.1.

Field intensity vs. arrival angle
Contoured transmission loss vs. depth and range
Contoured transmission loss vs. frequency and range
Individual mode functions vs. depth
Phase of acoustic field vs. depth
Sound speed vs. depth
Depth-averaged transmission loss vs. frequency
Depth-averaged transmission loss vs. range
Transmission loss vs. depth
Transmission loss vs. range

Table B.1   SNAP Outputs.

The environment, as shown in Figure B.1, is a half space divided into three layers: a water column of depth H_o , a sediment layer of thickness H_1 , and a semi-infinite subbottom. The sound speeds of the water column and sediment layer, $c_o(z)$ and $c_1(z)$, are allowed to vary arbitrarily with depth, while the densities, ρ_o and ρ_1 , and volume attenuations, β_o and β_1 , are held constant over depth. The subbottom is treated as a solid with constant shear speed, c_{2s} , shear attenuation, β_{2s} , compressional speed, c_2 , density, ρ_2 , and compressional attenuation, β_2 . These environmental parameters are allowed to vary with range by dividing the entire range into segments, each with different range-independent properties.
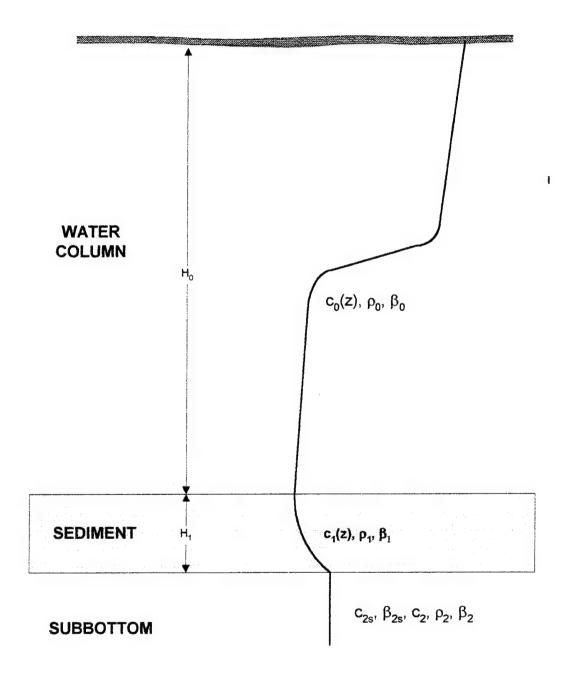
73

WATER COLUMN

H_0

$c_0(z),\ \rho_0,\ \beta_0$

SEDIMENT H_1 $c_1(z),\ \rho_1,\ \beta_1$

SUBBOTTOM $c_{2s},\ \beta_{2s},\ c_2,\ \rho_2,\ \beta_2$

Figure B.1 SNAP environmental model.

LIST OF REFERENCES

1. Hamson, R.M. and R.M. Heitmeyer, "Environmental and system effects on source localization in shallow water by the matched field processing of a vertical array," *J. Acoust. Soc. Am.* **86**, pp. 1951-1959, 1989.

2. Jesus, S.M., "Normal mode matching localization in shallow water: Environmental and system effects," *J. Acoust. Soc. Am.* **90**, pp. 2034-2041, 1991.

3. Hinich, M.J., "Array design for measuring source depth in a horizontal waveguide," *SIAM J. Appl. Math.* **32**, pp. 800-805, 1977.

4. Klemm, R., "Range and depth estimation by line arrays in shallow water," *Signal Process.* **3**, pp. 333-344, 1981.

5. Candy, J. and E. Sullivan, "Model-based passive ranging," *J. Acoust. Soc. Am.* **85**, pp. 2472-2480, 1989.

6. Zala, C.A. and J.M. Ozard, "Matched field processing in a range dependent environment," *J. Acoust. Soc. Am.* **88**, pp. 1011-1019, 1990.

7. Yang, T.C. and C.W. Bogart, "Matched-mode processing for sparse three-dimensional arrays," *J. Acoust. Soc. Am.* **95**, pp. 3149-3166, 1994.

8. Baggeroer, A.B., W.A. Kuperman and H. Schmidt, "Matched field processing: Source location in correlated noise as an optimum parameter estimation problem," *J. Acoust. Soc. Am.* **83**, pp. 571-587, 1988.

9. Smith, G.B., C. Feuillade and D.R. del Balzo, "Matched field processing enhancement in a shallow water environment by incoherent broadband averaging," *J. Acoust. Soc. Am.* **91**, pp. 1447-1455, 1992.

10. Dudgeon, D.E., "Fundamentals of digital array processing, " *Proc. IEEE* **65**, pp. 898-904, 1977.

11. Buker, H.P., "Use of calculated sound fields and matched field detection to locate sound sources in shallow water," *J. Acoust. Soc. Am.* **59**, pp. 368-373, 1976.

12. Tolstoy, A., *Matched Field Processing for Underwater Acoustics,* World Scientific, Singapore, 1993.

13. Yang, T.C., "Effectiveness of mode filtering: A comparison of matched field and matched mode processing," *J. Acoust. Soc. Am.* **87**, pp. 2072-2084, 1990.

14. Bogart, C.W. and T.C. Yang, "Comparative performance of matched mode and matched field processing in a range-dependent environment," *J. Acoust Soc. Am.* **92**, pp. 2051-2068,1992.

15. Bogart, W. and T.C. Yang, "Source localization with horizontal arrays in shallow water: Spatial sampling and effective aperture," *J. Acoust. Soc. Am.* **96**, pp. 1677-1686, September 1994.

16. Wilson, J.H. and J. Paquin, "Inverse Beamforming (IBF) for 3X Array Data," Neptune Sciences, Inc. Technical Report, October 1993.

17. Hamilton, E.L., "Geoacoustic modeling of the sea floor," *J. Acoust. Soc. Am.* **68**, pp. 1313-1340, 1980.

18. Hamilton, E.L., "Sound velocity and related properties of marine sediments," *J. Acoust. Soc. Am.* **72**, pp. 1891-1904, 1982.

19. A.C. Kibblewhite, "Attenuation of sound in marine sediments: A review with emphasis on new low frequency data," *J. Acoust. Soc. Am.* **86**, pp. 716-738, 1989.

20. Duarte, S., "A Comparative Study of Acoustic Models in a Shallow Water Range Independent Environment, " Masters Thesis, Naval Postgraduate School, Monterey, CA, 1994.

21. Naval Undersea Warfare Center Detachment, New London, CT, Report TR 10003, *Sonar Beamforming - An Overview Of Its History and Status*, by R.K. Knelpfer, 7 April 1992.

22. Burdic, W.S., *Underwater Acoustic System Analysis*, 2d ed., pp. 192-203, Prentice Hall, Inc., 1991.

23. Urick, R.J., *Principles of Underwater Sound*, 3rd ed., pp. 54-58, McGraw-Hill Book Co., Inc., 1983.

24. Nuttall, A.H. and J.H. Wilson, "Estimation of the acoustic field directionality by use of planar and volumetric arrays via the Fourier series method and the Fourier integral method," *J. Acoust. Soc. Am.* **81**, No. 1, October 1991.

25. Wilson, J.H., Memorandum from WAR, Inc., Tech. Rep. #1, May 1988.

26. Wilson, J.H. and P. Schey, "Beamforming and Spatial Prewhitening using the Fourier Series Method," Tech. Rep. #81, Polar Research Lab, Inc., 13 January 1988.

27. Nuttall, A.H., "Estimation of Noise Directionality Spectrum," NUSC Tech. Mem. TC-211-71, Naval Underwater Systems Center, New London, CT, 29 October 1971.

28. Nuttall, A.H., "Estimation of Noise Directionality Spectrum; Extensions and Generalizations, " NUSC Tech. Mem. TC-6-73, Naval Underwater Systems Center, New London, CT, 7 May 1973.

29. Wilson, J.H., "Signal Detection and Localization Using the Fourier Series Method (FSM) and Cross-Sensor Data," *J. Acoust. Soc. Am.* **73**, pp. 1648-1656, 1983.

30. Schmidt, R.O., "Multiple emitter location and signal parameter estimation," *IEEE Trans. Antennas Propagat.* **AP-34**, No. 3, March 1986.

31. Capon, J., "High-Resolution Frequency-Wavenumber Spectrum Analysis," *Proc. IEEE,* **57**, pp. 1408-1418, August 1969.

32. Porter M.B. and E.L. Reiss, "A numerical method for bottom interacting ocean acoustic normal modes," *J. Acoust. Soc. Am.* **77**, pp. 1760-1767, 1985.

33. Porter, M.B., "The KRAKEN normal mode program," Naval Research Laboratory Memorandum Report 5120-92-6920, Chap. 2, 1992.

34. Lim, P.H. and J.M. Ozard, "On the underwater acoustic field of a moving point source. I. Range-independent environment," *J. Acoust. Soc. Am.* **95**, pp. 131-137, January 1994.

35. Lim, P.H. and J.M. Ozard, "On the underwater acoustic field of a moving point source. II. Range-dependent environment," *J. Acoust. Soc. Am.* **95**, pp. 138-151, January 1994.

36. Hawker, K.E., "A normal mode theory of acoustic Doppler effects in the ocean waveguide," *J. Acoust. Soc. Am.* **65**, pp. 675-681, 1979.

37. Jensen, F.B. and M.C. Ferla, "SNAP: The SACLANTCEN NORMAL-MODE ACOUSTIC PROPAGATION MODEL," SACLANT ASW Research Centre, San Bartolomeo, Italy, 1979.

38. Naval Undersea Warfare Center Detachment, New London, CT, "CASS Sonar Manual," in preparation.

INITIAL DISTRIBUTION LIST

1. Defense Technical Information Center   2
   Cameron Station
   Alexandria, VA 22304-6145

2. Library, Code 52   2
   Naval Postgraduate School
   Monterey, CA 93943-5001

3. Chairman (Code PH/Cw)   3
   Department of Physics
   Naval Postgraduate School
   Monterey, CA 93943-5000

4. Chairman (Code OC/Bf)   3
   Department of Oceanography
   Naval Postgraduate School
   Monterey, CA 93943-5000

5. Dr. Ching-Sang Chiu (Code OC/Ci)   1
   Department of Oceanography
   Naval Postgraduate School
   Monterey, CA 93943-5000

6. Dr. James H. Wilson   6
   Neptune Sciences, Inc.
   3834 Vista Azul
   San Clemente, CA 92674

7. Ms. Josie Paquin-Fabre   2
   Neptune Sciences, Inc.
   150 Cleveland Ave.
   Slidell, LA 70458

8. Commander   1
   Naval Research Laboratory
   Code 7176
   Stennis Space Ctr, MS 39529
   ATTN: Dr. Ron Wagstaff

9. Mr. Barry Blumenthal   2
   Code C124A
   Advanced Environmental Acoustic Support Program
   Office of Naval Research
   800 N. Quincy St.
   Arlington, VA 22217-5660

10. Dr. Bill Cary   1
    ARPA/MSTO
    3701 N. Fairfax Drive
    Arlington, VA 22203-1714

11. LCDR Robert S. Veenhuis   1
    RR2 Box 2119
    Slayton, MN 56172

12. Mr. Ed Chaika / Mr. Dave Small   2
    Advanced Environmental Acoustic Support Program
    Code ONR-DET
    Building 1020 - Room 184
    Stennis Space Center, MS 39529-5000

13. Dr. R. Heitmeyer / Dr. T.C. Yang   2
    Naval Research Laboratory
    Code 5123
    Washington, DC 20375-5000

14. Commanding Officer   2
    NCCOSC RDTE DIV
    53560 Hull St.
    San Diego, CA 92152-5001
    ATTN: Frank Ryan/Dr. Homer Bucker

15. Commander, Submarine Developement Squadron 12   1
    NAVSUBASE New London
    Groton, CT 06349-5200
    ATTN: Master Chief Sonarman Stuckart

16. Commander, Submarine Developement Group 1   1
    139 Sylvester Road
    San Diego, CA 92106-3597

17. OIC SUBDEVGRU 1   1
    67 Wahoo Road
    NAVSUBASE Bangor
    Silverdale, WA 98315-0067

18. Commander, Submarine Group Five   1
    137 Sylvester Road
    San Diego, CA 92106-3521
    ATTN: Admiral Gustavson

19. Commander, Submarine Force U.S. Atlantic Fleet   1
    7958 Blandy Road
    Norfold, VA 23551-2492
    ATTN: N-2

20. Commander, Submarine Force U.S. Pacific Fleet   1
    Pearl Harbor, HI 96860-6550
    ATTN: N-2

21. Commander   2
    Naval Research Laboratory
    Code 7170
    Stennis Space Center, MS 32529
    ATTN: Mr. Jack McDermid

22. Mr. Jim Donald   1
    Naval Undersea Warfare Center
    New London Lab
    Code 01Y
    New London, CT 06320